Deciphering the origin of cyclical gravel front and shoreline progradation and retrogradation in the stratigraphic record

John J. Armitage[1], Peter A. Burgess[2], Gary J. Hampson[3], and Philip A. Allen[3]

[1]Department of Earth Science, Royal Holloway, University of London, Egham, UK; Now at Institut de Physique du Globe de Paris, 1 rue Jussieu, Paris, 75005, France; e-mail: armitage@ipgp.fr

[2]Department of Earth Science, Royal Holloway, University of London, Egham, UK

[3]Department of Earth Science and Engineering, Imperial College London, London, UK

May 4, 2016

Abstract

Nearly all successions of near-shore strata exhibit cyclical movements of the shoreline, which have commonly been attributed to cyclical oscillations in relative sea level (combining eustasy and subsidence) or, more rarely, to cyclical variations in sediment supply. It has become accepted that cyclical change in sediment delivery from source catchments may lead to cyclical movement of boundaries such as the gravel front, particularly in the proximal segments of sediment routing systems. In order to quantitatively assess how variations in sediment transport as a consequence of change in relative sea-level and surface run-off control stratigraphic architecture, we develop a simple numerical model of sediment transport and explore the sensitivity of moving boundaries within the sediment routing system to change in upstream (sediment flux, precipitation rate) and downstream (sea level) controls. We find that downstream controls impact the shoreline and sand front, while the upstream controls can impact the whole system depending on the amplitude of change in sediment flux and precipitation rate. The model implies that under certain conditions the relative movement of the gravel front and shoreline is a diagnostic marker of whether the sediment routing system experienced oscillations in sea level or climatic conditions. The model is then used to assess the controls on stratigraphic architecture in a well-documented palaeo–sediment-routing system in the Late Cretaceous Western Interior Seaway of North America. Model results suggest that significant movement of the gravel front is forced by pronounced ($\pm 50\,\%$) oscillations in precipitation rate. The absence of such movement in gravel front position in the studied strata implies that time-equivalent movement of the shoreline was driven by relative sea-level change. We suggest that tracking the relative trajectories of internal boundaries such as the gravel front and shoreline is a powerful tool in constraining the interpretation of stratigraphic sequences.

Keywords

sea-level, sediment flux, stratigraphy, modelling

1 Introduction

Change in sediment supply, sea level and subsidence are ubiquitously cited as the main controls on stratigraphic architecture (e.g. Vail et al., 1977; Van Wagoner et al., 1990; Catuneanu et al., 2009), but the extent to which any of these controls leave a unique signature within the stratigraphic record is not yet clear (e.g. Burgess et al., 2006; Burgess and Prince, 2015). Periodic changes in relative sea level may be accompanied by climatic change of the same periodicity if both sea level and climate are forced by Milankovitch orbital cycles. Such regional and global climatic cycles can have the effect of increasing or reducing surface run-off and sediment supply at the same time as changing sea-level (e.g. Blum and Hattier-Womack, 2009).

Sea-level change has clear implications for deposition within the coastal plain as the shoreline transits across this region. The response of the sediment routing system to shoreline migration likely decays upstream of the shoreline (e.g. Fisk, 1944; Blum and Törnqvist, 2000; Swenson, 2005). Down-stream of the shoreline the associated change in sediment flux into the submarine domain, along with change in water depth will determine stratal geometry, shoreline migration and generation of sequence stratigraphic boundaries (e.g. Heller et al., 1993; Burgess and Prince, 2015).

Climate change has less clear implications for sediment deposition. Periodic change in precipitation and surface water flow within the fluvial segment could amplify, damp and/or delay the sediment flux signal due the processes of sediment transport (Jerolmack and Paola, 2010; Simpson and Castelltort, 2012; Armitage et al., 2013; Godard et al., 2013; Braun et al., 2015). Furthermore, the timescale of sediment flux perturbation that may be recorded within the fluvial and deltaic segments is a function of the length of the sediment routing system (e.g. Dade and Friend, 1998; Métivier, 1999; Castelltort and Van Den Dreissche, 2003). It is therefore uncertain from a theoretical stand point whether sediment flux signals from the catchment can be transferred to the shoreline without modification. There is however some observational evidence from sediment routing systems that records of change in coastal to marine sediment accumulation are due to change in sediment flux from the catchment (Covault and Graham, 2010; Covault et al., 2011; Carvajal and Steel, 2012). If an upstream signal of increased sediment flux is transferred across the fluvial segment of the sediment routing system, then we could reasonably assume that it will supply more sediment to the shoreline and thus alter the shoreline trajectory.

The lack of a unique solution to the interpretation of stratigraphic architecture is a long standing problem within the methodology of sequence stratigraphy, and in the desire to understand how sediment accumulation is a record of past climate, tectonics and internal system dynamics. Previous studies have tried to gain an insight into how strata form using forward models of sediment transport (e.g. Burgess et al., 2006; Paola and Martin, 2012). From measuring the transfer of mass from sediment in transport to deposition from laboratory scale experiments, it has been observed that the application of idealised grain size sorting models may provide a way to analyse the movement of internal grain size boundaries within the sediment-routing systems (Paola and Martin, 2012). Therefore in order to quantitatively assess how variations in sediment transport due to change in relative sea level and surface run-off influence stratigraphic architectures, we will explore the sensitivity of such moving boundaries within a numerical sediment-routing system to change in upstream (sediment flux, precipitation rate) and downstream (sea level) controls. The internal boundaries that we focus on are (1) the downstream limit of alluvial conglomerates, the gravel front (Paola et al., 1992), (2) the shoreline, and (3) the down system limit of shallow marine sandstones, the sand front (Michael et al., 2013). These moving boundaries can be mapped within strata (e.g Michael et al., 2014; Hampson et al., 2014), and therefore have the potential to be used to diagnose past forcing of sediment-routing systems if it is known how they respond to change.

In this context we will explore three central questions:

(1) How sensitive are the positions of the gravel front, shoreline and sand front to sediment transport mechanisms. In other words, how closely linked via sediment transport are coastal plain, shelf and shoreline morphology and grain size distributions, and how does this linkage relate to control by sediment transport.

(2) What is the impact of upstream (sediment flux, precipitation rate) and downstream (sea level) controls on the positions of the gravel front, shoreline and sand front? The aim is to explore the uniqueness of relative sea-level control on shoreline position, implicit in many sequence stratigraphic interpretations. Experimental modelling will help to determine if there are signals upstream of the shoreline that can be used to differentiate driving mechanisms.

(3) Do the different parameters that influence shoreline position impart diagnostic characteristics to coastal plain and shelf stratigraphic architectures?

In the first part of the paper, we investigate these three questions using a generic model of a large sediment-routing system that contains both subaerial and subaqeous depositional domains. Sensitivity tests for the generic model establish a parameter space that is used to investigate a case study from the geological record. In the second part of the paper, we focus on a sediment-routing system within the Western Interior Basin, USA, in which stratal geometries, shoreline migration and sediment budget have been constrained for a period of approximately 6 Myr during the Late Cretaceous (Hampson, 2010; Hampson et al., 2014). The sediment-routing system represented by the Star Point Sandstone, Blackhawk Formation, lower part of the Castlegate Sandstone and coeval Mancos Shale is exposed in the Book Cliffs of east-central Utah and west-central Colorado, USA. These strata represent the birthplace of outcrop-scale sequence stratigraphy, and are widely visited by academic and industry groups to teach sequence stratigraphic methods and models; the Book Cliffs outcrops therefore provide an ideal case study with which to illustrate the importance of the three questions posed above.

2 Methods

We couple a 1-D model of sediment transport down depositional dip based on the flow of surface water to a 1-D model of deposition in the submarine domain (Figure 1). Subaerial sediment transport is modeled following Smith and Bretherton (1972) and Armitage et al. (2015), where we assume that sediment flux is a function of both local slope and surface water flux:

$$q_s = -\left(\kappa + c q_w^n\right) \frac{\partial z}{\partial x}, \tag{1}$$

where z is elevation, x is the down-system distance, κ is the linear diffusion coefficient, c is the fluvial transport coefficient, $n \geq 1$, and the water flux is given by,

$$q_w = \alpha x, \tag{2}$$

where α is the precipitation rate (see Table 1).

At the input boundary we introduce a sediment flux and a water flux, $q_w(in) = \alpha l_c$ to define the sediment transport at the left boundary (Figure 1). The catchment length, l_c, is assumed to be 150 km. We assume that the subaerial transport model extends from the proximal model boundary, which is the catchment outlet, to the shoreline. At this point we assume that the primary mechanism of sediment transport changes, and instead a combination of tidal and wave energy carries sediment farther down slope as a heuristic function of water depth (e.g. Kaufman et al., 1991),

$$q_s = -\kappa_{sea} e^{(-\kappa_{decay} abs(z_{sea} - z))} \frac{\partial z}{\partial x}, \tag{3}$$

where κ_{sea} is the linear diffusion coefficient for subaqueous sediment transport. κ_{decay} is the coefficient that parameterises the effect of water depth, z_{sea}, on subaqueous sediment transport (see Table 1; Kaufman et al., 1991). The change in elevation, z, is then given from the Exner equation of conservation of mass,

$$\frac{\partial z}{\partial t} = U - \frac{\partial q_s}{\partial x}, \tag{4}$$

Where U is uplift (positive) or subsidence (negative).

The sediment transport in the sediment-routing system is therefore described by a a non-linear diffusion equation in which the diffusion coefficient is a function of system length landward of the shoreline. Seaward of the shoreline the diffusion coefficient is a function of elevation. The system equation is solved iteratively using a simple finite element numerical model. From the initial condition, or previous time step, the diffusion coefficient is calculated given the relationship between elevation and sea level. To avoid sharp changes in diffusion coefficient that can cause numerical errors at the shoreline the diffusion coefficient is spatially smoothed using a moving average filter. Furthermore, to keep a stable solution where there is a strong contrast in diffusion coefficient the model resolution is increased in the vicinity of the shoreline. This results in the model being unable to generate a sharp break in slope at the shoreline.

Grain size is sorted down-system assuming first gravels, and then sand and finer grains are deposited (Armitage et al., 2015). The solution to the diffusion equation gives the topographic height for each point along the 1-D profile and hence the thickness of the deposits at a model time step. We then fill this slice of deposited mass with the gravel fraction, until there is none left. Subsequently the rest of the depositional thickness is filled with the sand and fines. The position at which gravel is exhausted in the model is therefore based on the assumption of perfect sorting as defined in Paola et al. (1992). Within the region of gravel deposition, the grain size is sorted down-system using the model of Fedele and Paola (2007). Below this point, the sand and fines are sorted following a Sternberg-type exponential sorting model (Sternberg, 1875; Robinson and Slingerland, 1998b).

The model domain is 5000 km long in the x-direction with an inflow boundary on the left hand side and fixed elevation on the right hand side (Figure 1). Subsidence is defined as either a spatially uniform rate, or a spatial distribution that matches the rate of accumulation inferred from observed thickness variations along a dip-oriented cross-section from studied strata in the Western Interior Basin. The model parameters are listed in Table 1.

3 Results of generic models

3.1 Effect of transport on position of shoreline and gravel front

In the first set of numerical experiments with the generic model domain, we explore how the sediment transport coefficients in the submarine domain control the position of the shoreline as surface run-off is increased within the subaerial domain. We assume that the gravel fraction of the source sediment supply is 10 %. For the subaerial domain we use the set of parameters that were found to approximate sediment transport within the Middle Miocene Escanilla sediment-routing system, which is a roughly 300 km long terrestrial to marine depositional sedimentary system in the Spanish Pyrenees (Table 1; Armitage et al., 2015). These values are chosen as they matched the patterns of sediment accumulation in the subaerial depositional domain of a sediment-routing system with a depositional length of c. 200 km. The linear diffusion coefficient κ in equation 1 only impacts sediment transport within the upper reaches of the catchment where it is larger in magnitude that the fluvial term, cq_w^n. The values of c and n were tuned to match the position of the gravel front in the Escanilla palaeo–sedimentary-routing system (Armitage et al., 2015). Given that the catchments of palaeo–sediment-routing systems have been removed by erosion, such that they cannot be directly observed, we will use these values for the hypothetical catchment. Subsidence is spatially uniform at a rate of $-0.5\,\mathrm{mm\,y^{-1}}$ (where positive values denote uplift), and $50\,\mathrm{m^2\,yr^{-1}}$ of sediment is fluxed into the proximal edge of the model domain at the left hand side.

From modelling a range of values for precipitation rate, α, and submarine transport coefficient κ_{sea}; $0.1 \leq \alpha \leq 2\,\mathrm{m\,yr^{-1}}$, and $10^4 \leq \kappa_{sea} \leq 10^5\,\mathrm{m^2\,yr^{-1}}$ in equations 1 and 3, we find that the final position of the gravel front and shoreline is a function of the transport rate in both subaerial and subaqueous depositional domains (Figure 2). The distance from the catchment outlet to the gravel front increases with increasing precipitation rate, as the input sediment flux is transported farther down slope. This increase in transport distance also causes progradation. The effect is modified, however, by the strength of the submarine transport coefficient, κ_{sea}, which defines the slope at the shoreline. The position of the gravel front is also clearly a function of the source gravel fraction (e.g. Marr et al., 2000; Armitage et al., 2015; Allen et al., 2015). We have assumed that the gravel fraction is constant in time. For this simple set-up of uniform subsidence, if the gravel fraction were 50 % larger at 15 % gravel then the gravel front is 10 % farther down-system and if likewise for a 50 % reduction the gravel front extends out to a 10 % shorter distance.

In addition to sediment flux, shoreline progradation or retrogradation is a function of the transport capacity of the submarine environment (Figure 3). There is an initial period of shoreline retreat as the initial surface become submerged due to the spatially uniform subsidence. If the magnitude of κ_{sea} is low then there is subsequently a steady progradation of the shoreline as the locus of deposition moves down system (Figure 3a; Table 2). If however κ_{sea} is high there is a steady retrogradation of the shoreline at a slower rate than the initial model evolution (Figure 3b; Table 2). This behaviour of the shoreline for high values of κ_{sea} is in the opposite sense to that of the contour of the 0.5 mm grain size (Figure 3b, white contours). This latter contour is a proxy for the sand front, and progrades for both values of κ_{sea} (Figure 3, white contours).

The positions of the gravel front and shoreline are also a function of the vertical profile of the submarine diffusion (Figure 4). This is because a decrease in κ_{decay} leads to an increase in the effective submarine sediment transport. Progradation or retrogradation of the shoreline position is a function of the transport capacity in the marine environment (Figure 5). In the case where κ_{decay} is $5 \times 10^3\,\mathrm{m}^{-1}$ (Figure 5a), the shoreline retreats throughout deposition of the modelled strata (Table 2), while the 0.5 mm grain size contour progrades seaward. Conversely for the case κ_{decay} is $5 \times 10^5\,\mathrm{m}^{-1}$ (Figure 5b, Table 2), the shoreline and sand front (0.5 mm grain size contour) both prograde as the model evolves. The positions of the shoreline and sand front are also in this latter case quite similar (Figure 5b).

Finally change in the transport rate within the submarine domain can effect deposition within the subaerial domain of the sediment-routing system. For $\kappa_{sea} = 5 \times 10^4\,\mathrm{m}^2\,\mathrm{yr}^{-1}$ and $\kappa_{decay} = 5 \times 10^3\,\mathrm{m}^{-1}$ (Figure 5a) the gravel front progrades at a rate of 8 km/Myr, which is twice as fast as the other four scenarios in Table 2. This model has the largest effective transport rate within the submarine domain, which results in the least change in slope at the shoreline (Figure 5a). By implication, patterns of subaerial deposition are expected to be more closely linked to those of subaqueous deposition in sediment-routing systems that are characterised by uniform gradients (i.e. ramps) than in those with pronounced breaks in slope (i.e. with shelf-slope clinoforms)

3.2 Oscillating sea level and precipitation rate

Under conditions of steady external forcing, the gravel front progrades as the sediment-routing system evolves and the shoreline either progrades or retrogrades depending on the rate of submarine diffusive transport. It is highly unlikely that precipitation rates and sea level remained steady over the multi-million year timescales represented by comparable stratal units in the geological record. Following in the footsteps of previous studies such as Paola et al. (1992) and Burgess et al. (2008), we therefore look at how the model responds to oscillating precipitation rates and relative sea-level. We assume a constant gravel fraction of 10 %.

Periodic change in precipitation rate causes a periodic response in the positions of the gravel front and shoreline (Figure 6). However, the time of maximum regression of the gravel front is slightly delayed with respect to the time of maximum precipitation rate. The shoreline migrates by a few kilometers as a function of a 10 % change in precipitation rate (Figure 6b). If, however, precipitation rate changes by 50 % then the delay in maximum gravel front regression relative to peak precipitation rate is increased (Figure 7a). The shoreline trajectory records cyclical progradation and retrogradation over a dip extent of 50 km, superimposed on overall progradation of the shoreline (Table 2). If precipitation rates oscillate by 50 % around their mean, then the periodicity and amplitude of shoreline migration is similar to those predicted in the model for a ± 10 m change in relative sea-level (Figure 6d and 7b; Table 2).

The numerical model suggests that the delay between the movement of the gravel front in response to precipitation signal is a function of the amplitude of the oscillation in precipitation rates, yet the delay in the periodic movement of the shoreline remains relatively unaffected by the amplitude of precipitation-rate oscillations (Figure 7c). This difference arises because the position of the gravel front is a function of the subaerial transport equations and its response time, τ, is an inverse function of precipitation rate (Armitage et al., 2013):

$$\tau \sim \frac{L^{2-n}}{c\alpha^n} \tag{5}$$

where L is the system length. Thus the response time of the gravel front is shorter for an increased precipitation rate. The shoreline position is however a function of transport in both subaerial and subaqueous regimes, and is therefore less dependent on the precipitation rate.

In contrast to the model results for oscillating precipitation rates, oscillations in relative sea-level of a magnitude of ± 10 m have no effect on the position of the gravel front, which lies far up system of the shoreline (Figure 6c, Table 2). The shoreline trajectory records cycles of progradation and retrogradation of a magnitude of 40-50 km, superimposed on an overall progradation of the shoreline similar to that observed in models without cyclical changes in relative sea-level (Figure 6d, 8 and 9, Table 2). The amplitude of shoreline migration due to relative sea-level change are relatively insensitive to subaerial sediment transport rate, and the shoreline migrates by similar amounts for a κ_{sea} of both 10^4 and 10^5 m^{2}yr^{-1} (Figures 8 and 9).

The modelled scenarios of change in relative sea-level and precipitation rate are both characterized by change in the spatial distribution of grain size, which oscillates in phase with the movement of the shoreline, (Figures 8 and 9). Depending on the subaerial transport rate, the

0.5 mm grain size contour, which approximates the sand front is predicted to lie either seaward of the shoreline ($\kappa_{sea} = 10^5$, Figure 8) or at a similar location to the shoreline ($\kappa_{sea} = 10^4$, Figure 9). The effects of changes in relative sea-level and precipitation rate are distinguished by the movement of the gravel front: change in relative sea-level has no impact on the gravel front position (Figures 8b and 9b), whereas change in precipitation rates has a clear impact on movement of the gravel front (Figures 8a and 9a).

3.3 Oscillating precipitation and input sediment flux

In addition to precipitation and relative sea-level, input sediment flux may also vary through time. The exact form of the response of sediment flux into the depositional system as a function of cyclical change in precipitation is uncertain (see Romans et al., 2015). To explore how the model behaves when both precipitation rates and sediment flux change we model two scenarios: (1) There is no change in precipitation rate and the input sediment flux oscillates (Figure 10 red line). (2) Precipitation rate and sediment flux oscillate in phase, by which we mean an increase in precipitation rate is coincident with an increase in input sediment flux (Figure 10 blue and black lines). As before, in these models we assume that the gravel fraction in the source remains constant at 10 %.

The effect of oscillations in input sediment flux by ±10 % of the mean value without a variation in precipitation rate is to cause an in-phase migration of the gravel front (Figure 10b and c, red lines). When the input sediment flux is increased the distance to the gravel front decreases and when the input sediment flux is decreased the distance to the gravel front increases (Figure 10c, red line). This can be explained by the increased input sediment flux requiring an increase in the slope at the proximal model boundary to transport the sediment. This therefore increases the area of deposits in the proximal domain causing a greater quantity of gravel to be extracted. Oscillations in the input sediment flux of ±10 % however have no effect on the shoreline (Figure 10d red line), as they are accommodated solely within the subaerial domain.

For a contemporaneous oscillation in precipitation rate of ±10 % magnitude and input sediment flux of ±10 % magnitude (Figure 10, blue lines) we find that conversely the location of the gravel front does not move through time (Figure 10c). This is because the response of the sediment-routing system to precipitation-rate changes are exactly the opposite to the response to changes in input sediment flux. An increase in precipitation rate increases the transport capacity and reduces the model slope, countering the increase in model slope due to the increase in input sediment flux. The shoreline trajectory is however sensitive to the precipitation rate change despite the oscillation in input sediment flux. This is because the shoreline is sufficiently far from the proximal region of the model to be unaffected by the change in input sediment flux. The shoreline trajectory records cyclic progradation and retrogradation over a dip extent of 20 km (Figure 10d and Figure 11).

The system response to a change in both input sediment flux and precipitation rate is therefore similar to that generated when only relative sea-level is altered (Figures 6, 8 and 9; Table 2), assuming that flux and precipitation rate cause relatively minor changes in the grain size distribution. A comparison of the predicted change in down system deposition for the same transport properties (Figures 8 and 11) shows that if input sediment flux increases with increasing precipitation, then there is a strong signal of oscillation in the position of the sand front and the shoreline, yet no movement in the gravel front other than overall progradation during the modelled time span (Figure 11a). This is remarkably similar to the model response to oscillating relative sea-level (Figure 8b). In contrast, if that amplitude of precipitation oscillations is greater than $\pm 10\,\%$ (Figure 10 black solid and dashed line), then the system response is similar to that when there is no change in input sediment flux (Figures 8a and 11b). Therefore, as the magnitude of precipitation-rate change is increased relative to the input sediment flux, the precipitation signal becomes dominant (Figure 10, black solid and dashed lines).

3.4 High frequency oscillations in precipitation rate

That there is a delay in maximum movement of the gravel front compared to maximum precipitation rate (Figure 7c) raises the possibility that high frequency (< 1 Myr periodicity) oscillations in precipitation rate would be buffered. To explore this possibility, we have run the model with periodic change in precipitation rate that defines 100, 200, 500 and 1000 kyr cycles (Figure 12). The delay in gravel front response is found to be a function of the forcing frequency (Figure 12c). However, the movement of the gravel front has a periodicity that is the same as the high frequency precipitation signal (Figure 12a and b). This shows that under these model assumptions the response recorded through the movement of the gravel front to a change in precipitation rate is out of phase but not buffered.

The phase shift relative to the period of the forcing is longer for shorter periodic change in precipitation rate (Figure 12c). As would be expected within this diffusive model, there is no destruction of the response by the transport system (see Jerolmack and Paola, 2010), however there is a delay in peak movement of the gravel front with respect to peak amplitude in precipitation rate. This may further complicate the interpretation of forcing mechanisms from the sedimentary record, when the modelled system responses are coupled with processes that operate over short timescales and are not captured by this model (e.g. Jerolmack and Paola, 2010; Simpson and Castelltort, 2012).

4 Application to Cretaceous sediment-routing system, Western Interior Seaway, USA

To test whether the model predictions have any value in interpreting real stratigraphic archives, we forward model aspects of Cretaceous alluvial, coastal plain and shallow marine strata exposed in the Book Cliffs of eastern Utah and western Colorado, USA. Here the proportions of gravel and sand have been estimated for the depositional system (Table 3; Hampson et al., 2014). These strata are also arguably the most documented and widely visited outcrop example of coastal plain and shallow marine strata that contain multiple, nested cycles of shoreline progradation and retrogradaiotn, yet the exact nature of the controls on shoreline migration is the subject of ongoing debate.

The investigated strata are the preserved record of a large palaeo–sediment-routing system that advanced into the foreland-to-intracratonic Upper Cretaceous Western Interior Basin of North America, in Utah and Colorado, USA (Figure 13). Predominantly siliciclastic sediment was eroded from the Sevier fold and thrust belt along the western margin of the basin, and transported eastwards into the Western Interior Seaway (Kauffman and Caldwell, 1993; DeCelles and Coogan, 2006). The sediment-routing system accumulated an eastward-thinning wedge of coastal plain to shallow marine strata that passes basin-ward into offshore shales, and which comprise the Star Point Sandstone, Blackhawk Formation, lower part of the Castlegate Sandstone and part of the Mancos Shale (Figures 13 and 14). This sediment-routing system is of late Santonian to Middle Campanian age ($84-78$ Ma), and occupied a subtropical palaeolatitude of c. 42 °N with a warm, humid climate throughout its deposition (Kauffman and Caldwell, 1993). Mean annual rainfall has been estimated to be of the order of $1.4\,\mathrm{m\,yr^{-1}}$ (p. 52-56 in Wolfe and Upchurch, 1987).

On a gross scale this system displays gradual progradation over its $5-6$ Myr duration (Figure 14; see Balsley, 1980; Hampson et al., 2012). This overall progradation is generally interpreted to record a progressive decrease in tectonic subsidence and accommodation (e.g. Taylor and Lovell, 1995; Adams and Battacharya, 2005; Hampson et al., 2012). At a smaller scale, shallow marine deposits are organised into eight stratigraphic intervals bounded by major flooding surfaces, with each interval representing a potential cycle of progradation and retrogradation (Figure 14; Hampson, 2010; Hampson et al., 2014). Each interval corresponds approximately to a shallow-marine member of the Blackhawk Formation, and has an estimated duration of $0.3-1.0$ Myr (Hampson et al., 2014). Several regressive-transgressive shallow-marine tongues (cf. parasequences) of c. $60-330$ kyr duration are progradationally to aggradationally stacked in each interval (cf. parasequence set). Multiple forcing mechanisms have been proposed for individual regressive-transgressive tongues and for intervals bounded by major flooding surfaces that contain stacked tongues: relative sea-level fluctuations that combine eustasy with tectonic subsidence (e.g. Van Wagoner et al., 1990; Kamola and Van Wagoner, 1995; Kamola and Huntoon, 1995; Houston et al., 2000), autogenic responses to lengthening of the coastal plain (Hampson, 2010), and variable sediment supply (Hampson et al., 2014). Herein we will use the eight stratigraphic intervals bounded by major flooding surfaces (Figure 14; Hampson et al., 2014) as a framework in which to explore how both sediment supply and relative sea-level may have influenced deposition within this ancient sediment-routing system.

Isopach maps and palaeogeographic reconstructions indicate that the Star Point – Blackhawk – lower Castlegate wedge is relatively uniform in thickness, facies composition and gross stratigraphic architecture for c. 200 km along depositional strike (NNE-SSW) at the scale of interest (e.g. Figure 13b; Hampson, 2010; Hampson et al., 2014). The sediment-routing system can therefore be simplified to a representative 2-D cross-section oriented WNW-ESE, as a first approximation. Sediment supply can then be considered in terms of fluvial influx from the left of the modelled cross-section, along the axis of the sediment-routing system, and net influx or net out flux of sediment from the shallow-marine domain of the modelled cross-section, perpendicular to the axis of the sediment-routing system (Hampson et al., 2014). The estimates of Hampson et al. (2014) indicate that only fine-grained sediment (silt, mud) was added or removed from the distal segments of the sediment-routing system by along-strike shallow-marine sediment transport, and the effects of this sediment transport can thus be mimicked for the perfect sorting assumption used here by varying the volume of fine-grained sediment in the fluvial sediment supply.

Our intention is not to reproduce the observed progradation of the Star Point – Blackhawk – lower Castlegate wedge, but to evaluate the controls on the gross architecture and stacking of the eight stratigraphic intervals (Figure 14). We adopt a similar approach to that used to model the Escanilla palaeo–sediment-routing system (Armitage et al., 2015), and take the observed stratal thickness plus an estimate of palaeo-water depth in the submarine depositional domain as a proxy for subsidence down the axis of the sediment-routing system (Table 3). Since information about the catchment is lacking we leave κ, c and n unchanged (see Table 1). We initiate the model with a subsidence profile as listed in Table 3, which serves to build a topographic slope that does not interfere with the subsequent model behaviour. κ_{sea} in equation 3 is $10^4\,\mathrm{m}^2\,\mathrm{yr}^{-1}$ and $\kappa_{decay} = 5{\times}10^4\,\mathrm{m}^{-1}$. The sediment flux and its gravel fraction during the eight time intervals (Table 3) is calculated from the observed depositional thickness and deposited sediment volumes (see Hampson et al., 2014 for details). The estimated errors in specific sediment volumes and their gravel, sand and shale fractions along the representative 2-D cross-section (Figure 14) are $\pm 26 - 37\,\%$ for each stratigraphic interval (after Table 1 in Hampson et al., 2014). These errors arise from uncertainty in the definition and thickness of stratigraphic intervals, and in the partitioning and textural characteristics of facies within the intervals. Uncertainty due to poor exposure of proximal strata that abut against the Charleston-Nebo Salient (Figure 14, after

Horton et al., 2004) contributes only approximately one third of the error in estimated sediment volumes and grain size fractions (Hampson et al., 2014). The gravel fraction in the youngest stratigraphic interval, which contains the Castlegate Sandstone, is significantly larger than in the underlying seven intervals (Table 3). Errors in sediment flux estimates are significantly larger, because age data are sparse. Nonetheless, the values summarised in Table 3 are first-order estimates that provide a plausible and internally consistent scenario (see Hampson et al., 2014 for discussion). Precipitation rate is initially $1.4\,\mathrm{m\,yr^{-1}}$ and is either held fixed through time, or changes by $\pm 50\,\%$ over a period of 2 Myr or 100 kyr. Sea level is likewise either held constant at an elevation of 0 m, or is oscillated by ± 10 m at a period of 2 Myr or 100 kyr.

In the absence of any oscillation in precipitation rate or relative sea-level the modelled sediment-routing system generates overall progradation of the shoreline (Figure 15a). Progradation of both the shoreline and sand front (0.5 mm grain size contour) occurs through all time intervals, with the exception of time interval 4, in which the high input sediment flux reduces the selective downstream fining such that the 0.5 mm grain size is not reached within the modelled domain (Figure 15a). The addition of a 2 Myr periodic change in relative sea-level of magnitude of ± 10 m (Figure 15b) or a 2 Myr periodic change in precipitation rate of magnitude $\pm 50\,\%$ (Figure 15c) does not significantly alter the modelled stratigraphic architecture, although the amplitude of shoreline migration is enhanced by a few 10's of kilometers at some major flooding surface (e.g. at FS400, between time intervals T6 and T7) compared to the model with no change in precipitation rate or relative sea-level (Figure 15).

Higher frequency change in relative sea-level and precipitation rate has a much clearer effect on the predicted stratigraphic architecture (Figure 16). Oscillations in relative sea level of ± 10 m at a period of 100 kyr cause migration of the shoreline and sand front over a dip extent of approximately 20 km (Figure 16a). As expected, the gravel front remains relatively unchanged by these oscillations in relative sea-level. Conversely, a 100 kyr periodic oscillation in precipitation rate of a magnitude of $\pm 50\,\%$ causes significant movement in the position of the gravel front, which exhibits cyclical progradations and retrogradation over a dip extent of approximately 70 km (Figure 16b). The movement of the sand front farther downstream is similar to that forced by changes in relative sea-level, yet there is less associated movement of the shoreline (Figure 16b). Movement of the sand front in the modelled strata cannot therefore be used as an observation that can distinguish between change in surface runoff or relative sea-level change.

Observed shifts in the position of the shoreline are of 20-40 km within the coastal to shallow-marine deposits (Figure 14). Such shifts can therefore be matched by the modelled high frequency oscillations in either precipitation rate or relative sea-level (Figure 16). The distinguishing factor is the pattern of coeval gravel front migration in upstream locations. The lower Castlegate Sandstone contains the gravel tongue that caps the Star Point – Blackhawk – lower Castlegate wedge (Figure 14). Cyclical change in run off would be expressed within the lower

Castlegate Sandstone by high-amplitude shifts in gravel front position (c.f. Figure 16). Although the lower Castlegate Sandstone contains some evidence of high frequency allogenic forcing, in the form of systematic vertical stacking of channel-belt sandstone bodies (McLaurin and Steel, 2007), it does not by any means provide definitive support for cyclical movement of the gravel front predicted by the idealised model. By implication the observed movement of the shoreline within the Star Point – Blackhawk – lower Castlegate wedge was more likely a consequence of high frequency change in relative sea-level, as inferred from other stratigraphic intervals and palaeographic locations in the Western Interior Seaway (e.g. Plint and Kreitner, 2007).

5 Discussion

Our numerical model implies that patterns in the relative movement of internal boundaries, the gravel front, shoreline and sand front, can be used to diagnose forcing mechanism(s) from observed stratigraphic architectures. The gravel front is strongly controlled by terrestrial sediment transport, and therefore if there is significant cyclical change in the surface flow of water then the gravel front responds via cyclical progradation and retrogradation (Figure 6). The timing of maximum regression of the gravel front will lag behind the peak increase in precipitation rate (e.g. by several tens to one hundred thousand years; Figure 7a and 12), yet this delay is most likely not observable given the age constraints available in most ancient stratigraphic records.

The shoreline and the sand front are sensitive to both terrestrial and submarine sediment transport (Figures 6 to 9). The magnitude of the cycles of shoreline and sand front progradation and retrogradation are a function of the precipitation rate change and the magnitude of relative sea-level change. A cyclical change in precipitation rates from 1.5 to $0.5\,\mathrm{m\,yr^{-1}}$ forces the shoreline and sand front to move by a similar magnitude as for a $\pm 10\,\mathrm{m}$ change in sea level (Table 2). This finding implies that movement of the shoreline and sand front cannot on their own be used as an indicator of change in relative sea level, and neither are they an indicator of change in sediment flux (Figure 8 and 9). The gravel front responds to a change in precipitation rate but is found to be insensitive to relative sea-level change. Movement of the gravel front is therefore potentially a powerful tool to diagnose forcing mechanisms of stratigraphic architecture, and to decipher past climatic change from sedimentary archives.

If however the input sediment flux from the catchment feeding the sediment-routing system changes along with the precipitation rate, then the gravel front is no longer a faithful recorder of change in surface run-off (Figure 11). Depending on the magnitude of change in input sediment flux and precipitation rate, the gravel front may not respond in a cyclical manner to the external forcing. This is because, within the construct of the model, the increase in area of sediment delivered from the catchment to the sediment-routing system is balanced by the increase in transport rate to move that material. Although it is possible that this balance in input sediment flux and transport only exists within simple idealised numerical models, the wider point is that multiple cyclical forcing mechanisms may counter each other. Given the complexity of sediment-routing systems, and the clear potential for autogenic behaviours to create cyclical patterns within stratal units (e.g. Hajek et al., 2010), the presence of cyclical movement of the gravel front and shoreline does not necessarily mean there was unsteady forcing by precipitation rate, input sediment flux or relative sea-level. That said, our model would suggest that change in the movement of the shoreline without movement in the gravel front is either a function of relative sea-level change, or of change in precipitation rate coupled with change in sediment delivery to the depositional sink. The simplest explanation would be the former, but it is important to stress that this is not a unique interpretation of the observed stratigraphic architecture.

In our generic model simulations we have assumed a constant gravel fraction in the sediment supply while oscillating input sediment flux and precipitation rate. It is plausible that, for example, increased precipitation can increase the fraction of gravel eroded within the source catchment (Allen et al., 2015). From previous numerical models it has been shown that such an increase in the coarse grain-size fraction coupled with increased precipitation rate increases the signal of progradation within the depostiional system (Armitage et al., 2011). When exploring the sensitivity of the gravel front to gravel fraction we found that a $\pm 50\,\%$ difference in gravel fraction moves the location of the gravel front by $\pm 10\,\%$. In applying our model to a geological location we however make the assumption that the fraction of gravel and sand within the deposits of the sediment-routing system is representative of the source. We suggest that this assumption limits the potential for misinterpretation of the model relative to the observed stratigraphic record.

When this model is applied to the Star Point – Blackhawk – lower Castlegate – Mancos sediment-routing system, based on the interpretation outlined in Table 3, we find that the overall progradational stratigraphic architecture can be readily matched. High-frequency changes in sea level and/or precipitation rate, of a period of 100 kyr, have a clear effect on migration of the shoreline and sand front (Figure 16). If we assume that the observed depositional thickness of sediment is representative of the sediment flux into the basin, then the migration history of the gravel front would be a quantifiable measure to distinguish whether cyclical patterns of progradation and retrogradation were the result of cyclical change in precipitation rates or sea level (Figure 16). Data describing the architecture of proximal deposits in the Star Point – Blackhawk – lower Castlegate – Mancos sediment-routing system are rare, however on balance the evidence suggests limited movement of the gravel front. Therefore, a high-frequency cyclical change in relative sea-level is the most probable of modelled mechanisms to account for the observed stratigraphic architecture.

We estimated the potential error in the observed gravel, sand, and shale fractions to be of the order of $\pm 30\,\%$. Therefore, we could be either overestimating or underestimating the position of the gravel front by no more than $\pm 10\,\%$ of the depositional length of the sediment routing system (i.e. by up to $\pm 40\,\mathrm{km}$). When comparing the model to the observed stratigraphic section it is worth explaining that we are interested in matching the trend, or relative change in the position of the moving boundary as well as the magnitude. Therefore, error in our interpretation would be introduced only if we make a non-systematic error in accounting for the deposited sediment.

The predicted location of the shoreline is a function of the water flux, the sediment transport coefficient (c in equation 1) and the sea level. We assume that the transport coefficient is independent of grain size. While such a transport coefficient is potentially grain size dependent (e.g. Marr et al., 2000), at large distances down the subaerial system the overall diffusion coefficient for the Exner balance is dominated by the water flux. This is because for large x, $q_w^n >> c$ in equation 1. Therefore, it is reasonable to suggest that the predicted topography at large values of x and hence shoreline is not strongly altered by the fraction of gravel, sand and finer grains within the sediment source. Therefore, while the model presented is a simplification of the complex processes of sediment transport and deposition, we propose that the results are most likely valid and remain useful for interpreting the stratigraphic record.

6 Conclusions

We have developed a simple non-linear diffusive model of sediment transport to explore how cyclical changes in sediment delivery, surface run-off (precipitation rate) and relative sea-level effect stratigrahic architecture. In particular, we have focused on how change in these external drivers influence the movement of internal depositional boundaries: the gravel front, the shoreline and the sand front. The subaerial and subaqueous domains have a greater linkage in terms of delivery of sediment from source to sink for a higher transport rate in the marine system. The increased transport rate leads to ramp-like stratigraphic architecture, rather than clinoforms. Furthermore, in the generic application of the model where subsidence is constant in time and uniform in space, we find that change in sediment transport in the subaqueous domain does not significantly impact the terrestrial domain, i.e. the gravel front. However, change in sediment transport in the subaerial domain impacts the whole system including the shoreline and sand front, which typically rests basinwards of the shoreline.

The results of the numerical model imply that change in precipitation rate and change in relative sea-level generate diagnostically different responses in movement of the gravel front. Both mechanisms force the shoreline and sand front to move by similar distances, yet it is only when precipitation rate changes that the gravel front responds. This simple diagnostic response is then modified when the sediment flux delivered to the sediment-routing system is also cyclically changed with the change in precipitation rates. If both input sediment flux and precipitation rates change in phase, then movement of the gravel front can be greatly reduced to give similar patterns of deposition as those that result from relative sea-level change.

The lack of a unique diagnostic measure for the forcing mechanisms of ancient sediment-routing systems can be overcome if the input sediment flux from the catchment can be measured independently. This can be achieved if the majority of the depositional system is preserved, allowing for a sediment budget to be calculated. By applying the model to the deposits of such a sediment-routing system, the Cretaceous Star Point – Blackhawk – lower Castlegate – Mancos system exposed in the Book Cliffs of Utah and Colorado, we find that cyclical progradation and retrogradation of the shoreline and sand front can be a consequence of either oscillating precipitation rate or relative sea-level. Movement of the gravel front becomes the diagnostic indicator of forcing of the sediment-routing system by an upstream (sediment flux, precipitation rate) or downstream (relative sea-level) control.

Acknowledgments

This work was funded by a Royal Astronomical Society Research Fellowship awarded to John Armitage. We thank Cynthia Ebinger, Teresa Jordan and an anonamous reviewer for their time and comments that improved this manuscript.

Conflict of interest section

No conflict of interest declared.

References

Adams, M. M., Battacharya, J. P., 2005. No change in fluvial style across a sequence boundary, Cretaceous Blackhawk and Castlegate Formations of central Utah, USA. Journal of Sedimentary Research 75, 1038–1051, doi: 10.2110/jsr.2005.080.

Allen, P. A., Armitage, J. J., Whittaker, A. C., Michael, N. A., Roda-Boluda, D., D'Arcy, M., 2015. Fragmentation model of the grain size mix of sediment supplied to basins. Journal of Geology 123, 405–427, doi: 10.1086/683113.

Armitage, J. J., Allen, P. A., Burgess, P. M., Hampson, G. J., Whittaker, A. C., Duller, R. A., Michael, N. A., 2015. Physical stratigraphic model for the Eocene Escanilla sediment routing system: Implications for the uniqueness of sequence stratigraphic architectures. Journal of Sedimentary Research 85, 1510–1524, doi: 10.2110/jsr.2015.97.

Armitage, J. J., Duller, R. A., Whittaker, A. C., Allen, P. A., 2011. Transformation of tectonic and climatic signals from source to sedimentary archive. Nature Geoscience 4, 231–235, doi: 10.1038/ngeo1087.

Armitage, J. J., Dunkley Jones, T., Duller, R. A., Whittaker, A. C., Allen, P. A., 2013. Temporal buffering of climate-driven sediment flux cycles by transient catchment response. Earth and Planetary Science Letters 369-370, 200–210, doi: 10.1016/j.epsl.2013.03.020.

Balsley, J. K., 1980. Cretaceous wave-dominated delta systems, Book Cliffs, east-central Utah. Continuing Education Course Field Guide. American Association of Petroleum Geologists.

Blum, M. D., Hattier-Womack, J., 2009. Climate change, sea-level change, and fluvial sediment supply to deepwater depositional systems. In: Kneller, B. C., Martinsen, O. J., McCaffrey, B. (Eds.), External Controls on Deep-Water Depositional Systems. SEPM Special Publication 92. SEPM, Tulsa, Oklahoma, pp. 15–39.

Blum, M. D., Törnqvist, T. E., 2000. Fluvial responses to climate and sea-level change: a review and look forward. Sedimentology 47 (Suppl. 1), 2–48, doi: 10.1046/j.1365-3091.2000.00008.x.

Braun, J., Voisin, C., Gourlan, A. T., Chauvel, C., 2015. Erosional response of an actively uplifting mountain belt to cyclic rainfall variations. Earth Surface Dynamics 3, 1–14, doi: 10.5194/esurf-3-1-2015.

Burgess, P. M., Lammers, H., Van Oosterhout, C., Granjeon, D., 2006. Multivariate sequence stratigraphy: tackling complexity and uncertainty with stratigraphic forward modelling, multiple scenarios, and conditional frequency maps. American Association of Petroleum Geologists Bulletin 90, 1883–1901, doi: 10.1306/06260605081.

Burgess, P. M., Prince, G. D., 2015. Non-unique stratal geometries: implications for sequence stratigraphic interpretations. Basin Research 27, 351–365, doi: 10.1111/bre.12082.

Burgess, P. M., Steel, R., Granjeon, D., 2008. Stratigraphic forward modeling of basin-margin clinoform systems: Implications for controls on topset and shelf width and timing of formation of shelf-edge deltas. In: Recent Advances in Models of Siliciclastic Shallow-Marine Stratigraphy. Vol. 90 of SEPM Special Publication. Society for Sedimentary Geology, pp. 35–45.

Carvajal, C., Steel, R., 2012. Source-to-sink sediment volumes within a tectono-stratigraphic model for a Laramide shelf-to-deep-water basin: Methods and results. In: Busby, C., Azor Perez, A. (Eds.), Tectonics of Sedimentary Basins: Recent Advances. Wiley-Blackwell, Oxford, UK, pp. 131–151.

Castelltort, S., Van Den Dreissche, J., 2003. How plausible are high-frequency sediment supply-driven cycles in the stratigraphic record? Sedimentary Geology 157, 3–13, doi: 10.1016/S0037-0738(03)00066-6.

Catuneanu, O., Abreu, V., Bhattacharya, J. P., Blum, M. D., Dalrymple, R. W., Eriksson, P. G., Fielding, C. R., Fisher, W. L., Galloway, W. E., Gibling, M. R., Gilesk, K. A., Holbrook, J. M., Jordan, R., Kendall, C. G., Macurda, B., Martinsen, O. J., Miall, A. D., Neal, J. E., Nummeda, D., Pomar, L., Posamentier, H. W., Pratt, B. R., Sarg, J. F., Shanley, K. W., Steel, R. J., Strasser, A., Tucker, M. E., Winker, C., 2009. Towards the standardization of sequence stratigraphy. Earth-Science Reviews 92, 1–33, doi: 10.1016/j.earscirev.2008.10.003.

Covault, J. A., Graham, S. A., 2010. Submarine fans at all sea-level stands: Tectono-morphologic and climatic controls on terrigenous sediment delivery to the deep sea. Geology 38, 939–942, doi: 10.1130/G31081.1.

Covault, J. A., Romans, B. W., Graham, S. A., Fildani, A., Hilley, G. E., 2011. Terrestrial source to deep-sea sink sediment budgets at high and low sea levels: Insights from tectonically active southern California. Geology 39, 619–622, doi: 10.1130/G31801.1.

Dade, W. B., Friend, P. F., 1998. Grain-size, sediment-transport regime, and channel slope in alluvial rivers. Journal of Geology 106, 661–675, doi: 10.1086/516052.

DeCelles, P. G., Coogan, J. C., 2006. Regional structure and kinematic history of the Sevier fold-and-thrust belt, central Utah. Geological Society of America, Bulletin 118, 841–864, doi: 10.1130/B25759.1.

Fedele, J. J., Paola, C., 2007. Similarity solutions for alluvial sediment fining by selective deposition. Journal of Geophysical Research 112 (F02038), doi: 10.1029/2005JF000409.

Fisk, H. N., 1944. Geological investigation of the alluvial valley of the lower Mississippi River. War Department, Corps of Engineers, p. 78.

Godard, V., Tucker, G. E., Burch Fisher, G., Burkbank, D. W., Bookhagen, B., 2013. Frequency-dependent landscape response to climatic forcing. Geophysical Research Letters 40, 859–863, doi: 10.1002/grl.50253.

Hajek, E. A., Heller, P. L., Sheets, B. A., 2010. Significance of channel-belt clustering in alluvial basins. Geology 38, 535–538, doi: 10.1130/G30783.1.

Hampson, G. J., 2010. Sediment dispersal and quantitative stratigraphic architecture across an ancient shelf. Sedimentology 57, 96–141, doi: 10.1111/j.1365-3091.2009.01093.x.

Hampson, G. J., Duller, R. A., Petter, A. L., Robinson, R. A. J., Allen, P. A., 2014. Mass-balance constraints on stratigraphic interpretation of linked alluvialcoastalshelfal deposits from source to sink: Example from Cretaceous Western Interior Basin, Utah and Colorado, USA. Journal of Sedimetary Research 84, 935–960, doi: 10.2110/jsr.2014.78.

Hampson, G. J., Royhan Gani, M., Sahoo, H., Rittersbacher, A., Irfan, N., Ranson, A., Jewell, T. O., Gani, N. D. S., Howell, J. A., Buckley, S. J., Bracken, B., 2012. Alluvial-to-coastal plain stratigraphic architecture and large-scale patterns of fluvial sandbody distribution in a progradational clastic wedge: Upper Cretaceous Blackhawk Formation, Wasatch Plateau, central Utah, USA. Sedimentology 59, 2226–2258, doi: 10.1111/j.1365-3091.2012.01342.x.

Heller, P. L., Burns, B. A., Marzo, M., 1993. Stratigraphic solution sets for determining the roles of sediment supply, subsidence and sea level on transgressions and regressions. Geology 21, 747–750, doi: 10.1130/0091-7613(1993)021<0747:SSSFDT>2.3.CO;2.

Horton, B. K., Constensius, K. N., DeCelles, P. G., 2004. Tectonic control on coarse-grained foreland-basin sequences: an example from the Cordilleran foreland basin, Utah. Geology 32, 637–640, doi: 10.1130/G20407.1.

Houston, W. S., Huntoon, J. E., Kamola, D. L., 2000. Modeling of cretaceous foreland-basin parasequences, utah, with implications for timing of sevier thrusting. Geology 28, 267–270, doi: 10.1130/0091-7613(2000)28<267:MOCFPU> 2.0.CO;2.

Jerolmack, D. J., Paola, C., 2010. Shredding of environmental signals by sediment transport. Geophysical Research Letters 37 (L19401), doi: 10.1029/2010GL044638.

Johnson, R. C., 2003. Depositional framework of the Upper Cretaceous Mancos Shale and the lower part of the Upper Cretaceous Mesaverde Group, Western Colorado and Eastern Utah. In: Petroleum Systems and Geologic Assessment of Oil and Gas in the UintaPiceance Province, Utah and Colorado. No. DDS-69-B in Digital Data Series. U.S. Geological Survey, Ch. 10.

Kamola, D. L., Huntoon, J. E., 1995. Repetitive stratal patterns in a foreland basin sandstone and their possible tectonic significance. Geology 23, 177–180, doi: 10.1130/0091-7613(1995)023<0177:RSPIAF> 2.3.CO;2.

Kamola, D. L., Van Wagoner, J. C., 1995. Stratigraphy and facies architecture of parasequences with examples from spring Canyon Member, Blackhawk Formation, Utah. In: Van Wagoner, J. C., Bertram, G. T. (Eds.), Sequence Stratigraphy of Foreland Basin Deposits. No. 64 in Memoir. American Association of Petroleum Geologists, pp. 27–54.

Kauffman, E. G., Caldwell, W. G. E., 1993. The western interior basin in space and time. In: Caldwell, W. G. E., Kauffman, E. G. (Eds.), Evolution of the Western Interior Basin. Special Paper, 39. Geological Association of Canada, pp. 1–30.

Kaufman, P., Grotzinger, J. P., McCormick, D. S., 1991. Depth-dependent diffusion algorithm for simulation of sedimentation in shallow marine depositional systems. Bulletin - Kansas Geological Survey 233, 489–508.

Krystinik, L. F., DeJarnett, B. B., 1995. Lateral variability of sequence stratigraphic framework in the Campanian and Lower Maastrichtian of the Western Interior Seaway. In: Van Wagoner, J. C., Bertram, G. T. (Eds.), Sequence Stratigraphy of Foreland Basin Deposits. No. 64 in Memoir. American Association of Petroleum Geologists, pp. 11–26.

Marr, J. G., Swenson, J. G., Paola, C., Voller, V. R., 2000. A two-diffusion model of fluvial stratigraphy in closed depositional basins. Basin research 12, 381–398, doi: 10.1046/j.1365-2117.2000.00134.x.

McLaurin, B. T., Steel, R. J., 2000. Fourth-order nonmarine to marine sequences, Middle Castlegate Formation, Book Cliffs, Utah. Geology 28, 359–362.

McLaurin, B. T., Steel, R. J., 2007. Architecture and origin of an amalgamated fluvial sheet sand, lower Castlegate Formation, Book Cliffs, Utah. Sedimentary Geology 197, 291–311, doi: 10.1016/j.sedgeo.2006.10.005.

Métivier, F., 1999. Diffusivelike buffering and saturation of large rivers. Physical Review E 60, 5827–5832.

Michael, N. A., Whittaker, A. C., Allen, P. A., 2013. The functioning of sediment routing systems using a mass balance approach: Example from the Eocene of the Southern Pyrenees. Journal of Geology 121 (581-606), doi: 10.1086/673176.

Michael, N. A., Whittaker, A. C., Carter, A., Allen, P. A., 2014. Volumetric budget and grain-size fractionation of a geological sediment routing system: Eocene Escanilla Formation, south-central Pyrenees. Geological Society of America Bulletin 126, 585–599, doi: 10.1130/B30954.1.

Obradovich, J. D., 1993. A Cretaceous time scale. In: Caldwell, W. G. E., Kauffman, E. G. (Eds.), Evolution of the Western Interior Basin. Special Paper, 39. Geological Association of Canada, pp. 379–378.

Paola, C., Heller, P. L., Angevine, C. L., 1992. The large-scale dynamics of grain-size variation in alluvial basins, 1: Theory. Basin Research 4, 73–90, doi: 10.1111/j.1365-2117.1992.tb00145.x.

Paola, C., Martin, J. M., 2012. Mass-balance effects in depositional systems. Journal of Sedimentary Research 82, 435–450, doi: 10.2110/jsr.2012.38.

Plint, A. G., Kreitner, M. A., 2007. Extensive thin sequences spanning cretaceous foredeep suggest high-frequency eustatic control: Late Cenomanian, Western Canada foreland basin. Geology 35, 735–738, doi: 10.1130/G23662A.1.

Robinson, R. A. J., Slingerland, R. L., 1998a. Grain-size trends, basin subsidence and sediment supply in the Campanian Castlegate Sandstone and equivalent conglomerates of central Utah. Basin Research 10, 109–127.

Robinson, R. A. J., Slingerland, R. L., 1998b. Origin of fluvial grain-size trends in a foreland basin: the Pocono Formation on teh Central Appalachian Basin. Journal of Sedimentary Research 68, 473–486.

Romans, B. W., Castelltort, S., Covault, J. A., Fildani, A., Walsh, J. P., 2015. Environmental signal propagation in sedimentary systems across timescales. Earth Science Reviews doi: 10.1016/j.earscirev.2015.07.012.

Simpson, G., Castelltort, S., 2012. Model shows that rivers transmit high-frequency climate cycles to the sedimentary record. Geology 40, 1131–1134, doi: 10.1130/G33451.1.

Smith, T. R., Bretherton, F. P., 1972. Stability and conservation of mass in drainage basin evolution. Water Resources Research 8, 1506–1529, doi: 10.1029/WR008i006p01506.

Sternberg, H., 1875. Untersuchungen über Längen und Querprofil geschiebeführnde Flüsse. Zeitschrift fur das Bauwesen 25, 483–506.

Swenson, J. B., 2005. Relative importance of fluvial input and wave energy in controlling the timescale for distributary-channel avulsion. Geophysical Research Letters 32, L23404, doi: 10.1029/2005GL024758.

Taylor, D. R., Lovell, R. W. W., 1995. High-frequency sequence stratigraphy and paleogeography of the Kenilworth member, Blackhawk Formation, Book Cliffs, Utah, U.S.A. In: Van Wagoner, J. C., Bertram, G. T. (Eds.), Sequence Stratigraphy of Foreland Basin Deposits. No. 64 in Memoir. American Association of Petroleum Geologists, pp. 257–275.

Vail, P. R., Mitchum Jr., R. M., Todd, R. G., Widmier, J. M., Thompson III, S., Sangee, J. B., Bubb, J. N., Hatlelid, W. G., 1977. Seismic stratigraphy and global changes of sea–level. In: Payton, C. E. (Ed.), Seismic StratigraphyApplications to Hydrocarbon Exploration. Vol. 26 of American Association of Petroleum Geologists Memoir. AAPG, pp. 49–212.

Van Wagoner, J. C., Mitchum, R. M., Campion, K. M., Rahmanian, V. D., 1990. Siliciclastic sequence stratigraphy in well logs, cores, and outcrops. Vol. 7 of Methods in Exploration. Association of Petroleum Geologists, 55 p.

Wolfe, J. A., Upchurch, G. R., 1987. North american nonmarine climates and vegetation during the late cretaceous. Palaeogeography, Palaeoclimatology, Palaeoecology 61, 33–77, doi: 10.1016/0031-0182(87)90040-X.

Tables

Table 1: List of model parameters.

Table 2: Gravel front and shoreline trajectory analysis.

Table 3: Model input conditions for application to the Star Point – Blackhawk – lower Castlegate – Mancos sediment-routing system.

Figures

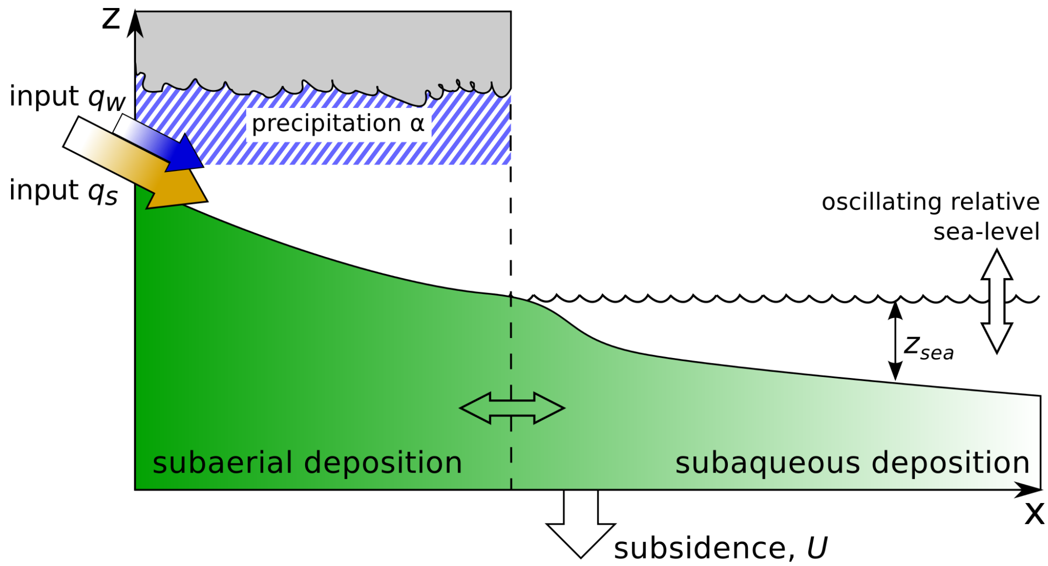

Figure 1: Diagram of model domain. On the left are the input sediment flux, q_s, and input water flux, q_w, which is a function of the precipitation rate multiplied by the catchment length (assumed to be 150 km). At the base, accommodation space is generated though a spatial distribution of subsidence, U. In the subaerial domain, sediment transport is a function of slope and precipitation rate, α, see equation 1 and 2. In the subaqueous domain sediment transport is a function of water depth, z_{sea}, see equation 3. The boundary between these domains is a function of elevation and relative sea-level, and is free to move depending on the transport of sediment.

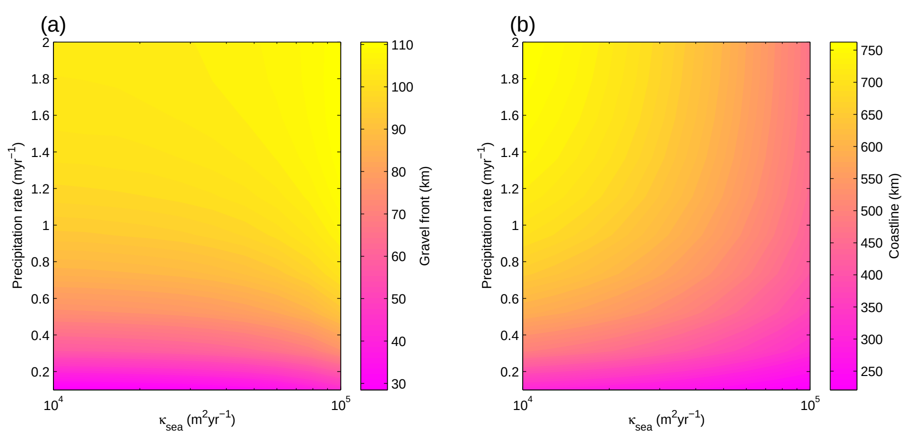

Figure 2: Plots of the down system positions of (a) the gravel front and (b) the shoreline after 10 Myr of model evolution, as a function of model precipitation rate, α (Equation 2) and the magnitude of κ_{sea} within the submarine diffusive transport equations (Equation 3).

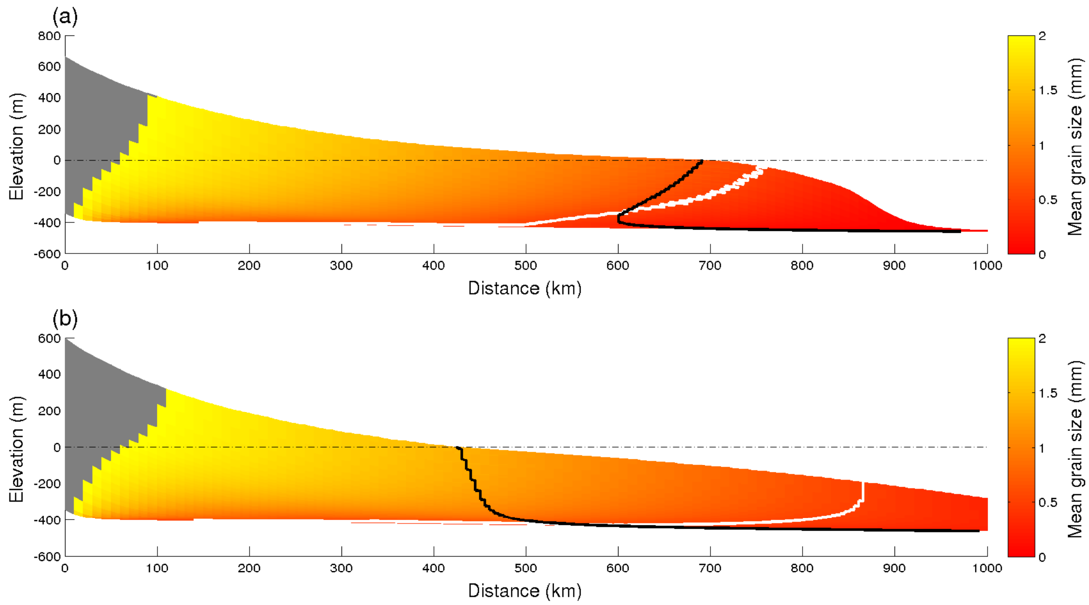

Figure 3: Model stratigraphic cross-sections for two values of κ_{sea} (Equation 3). κ_{decay} (Equation 3) is held constant at $5 \times 10^4\,\mathrm{m}^{-1}$. (a) Grain size deposited for a model where $\kappa_{sea} = 10^4\,\mathrm{m}^2\mathrm{yr}^{-1}$, with spatially uniform subsidence at $0.5\,\mathrm{mm\,yr}^{-1}$. Precipitation rate is $1\,\mathrm{m\,yr}^{-1}$ and the input sediment flux is $50\,\mathrm{m}^2\mathrm{yr}^{-1}$ on the left model boundary. Regions of gravel grains are blocked out in gray. The mean grain size of grains finer than 2 mm in diameter is plotted, with the grain size of 0.5 mm displayed as a white contour that approximates the sand front. The shoreline position through time is marked as a solid black line, and the dashed black line marks sea level. (b) Grain size deposited where $\kappa_{sea} = 10^5\,\mathrm{m}^2\mathrm{yr}^{-1}$.

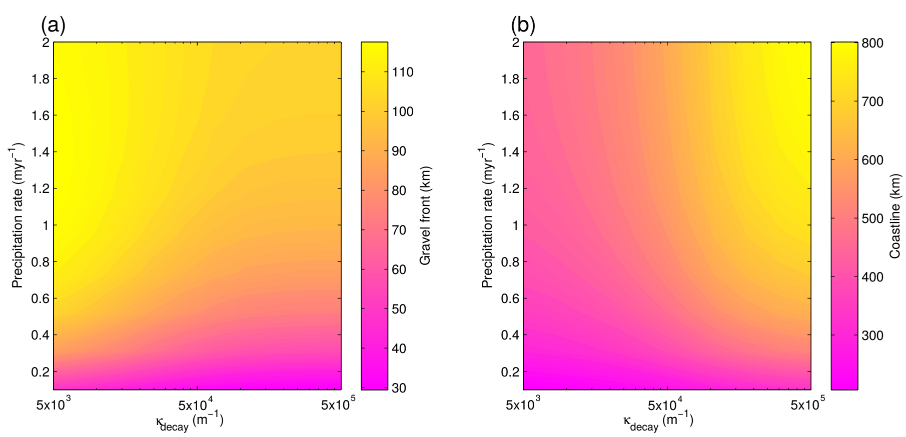

Figure 4: Plots of the down system position of (a) the gravel front and (b) the shoreline after 10 Myr of model evolution, as a function of model precipitation rate, α (Equation 2) and the magnitude of κ_{decay} within the submarine diffusive transport equations (Equation 3).

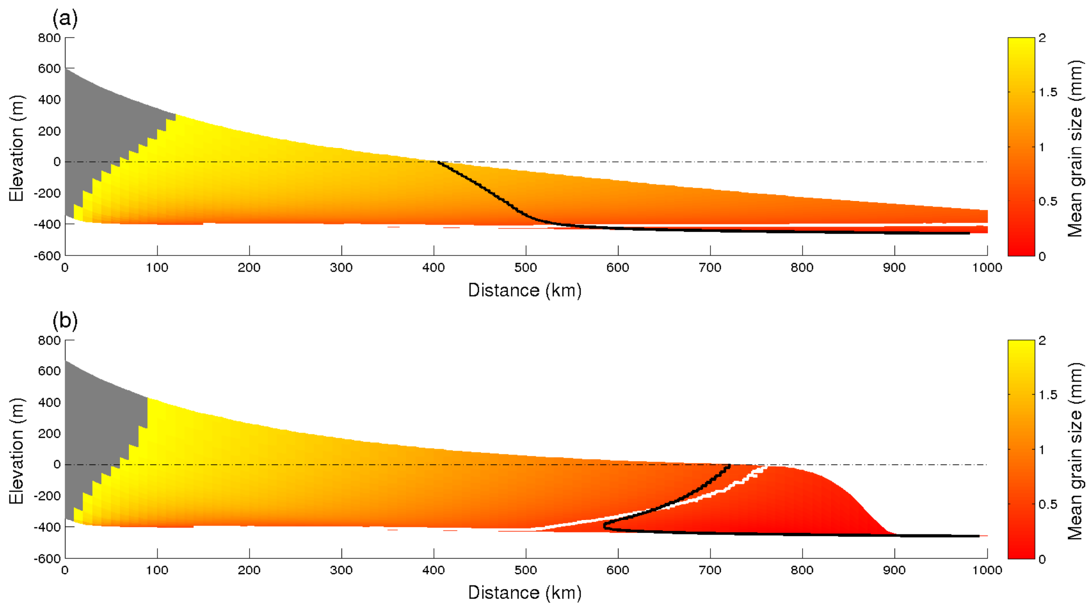

Figure 5: Model stratigraphic sections for two values of κ_{decay} (Equation 3). κ_{sea} (Equation 3) is held constant at $5 \times 10^4\,\mathrm{m^2 yr^{-1}}$. (a) Grain size deposited for a model where $\kappa_{decay} = 5 \times 10^3\,\mathrm{m^{-1}}$, with spatially uniform subsidence at $0.5\,\mathrm{mm\,yr^{-1}}$. Precipitation rate is $1\,\mathrm{m\,yr^{-1}}$ and the input sediment flux is $50\,\mathrm{m^2yr^{-1}}$ on the left model boundary. Regions of gravel grains are blocked out in gray. The mean grain size of grains finer than 2 mm in diameter is plotted, with the grain size of 0.5 mm displayed as a white contour that approximates the sand front. The shoreline position through time is marked as a solid black line, and the dashed black line marks sea level. (b) Grain size deposited where $\kappa_{decay} = 5 \times 10^5\,\mathrm{m^{-1}}$.

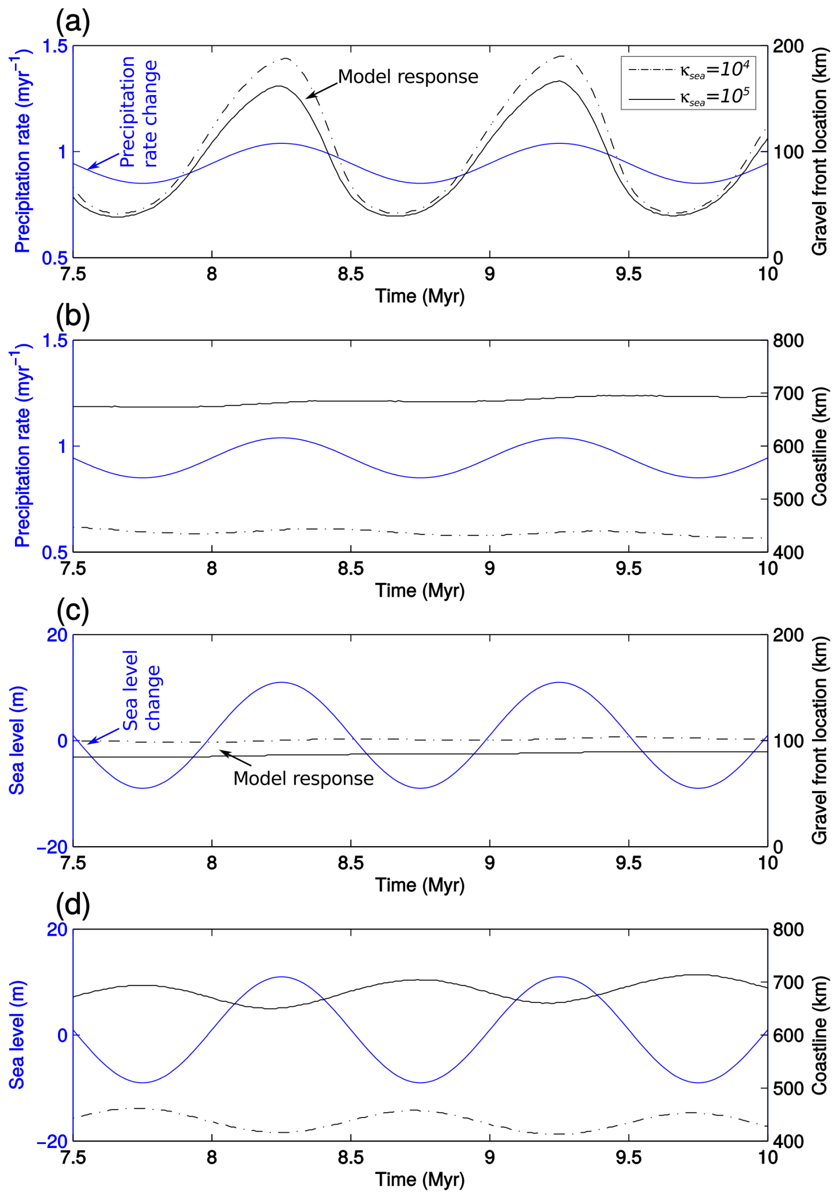

Figure 6: Response of the sediment transport model where $\kappa_{sea} = 10^4\,\mathrm{m}^2\mathrm{yr}^{-1}$ (dashed black lines) and $\kappa_{sea} = 10^5\,\mathrm{m}^2\mathrm{yr}^{-1}$ (solid black lines) to oscillating precipitation rates at $\pm 10\,\%$ of the mean or sea level with a period of 1 Myr and an amplitude of ± 10 m (blue lines). (a) Movement of the position of the gravel front as a consequence of change in precipitation rates. (b) Movement of the shoreline as a consequence of change in precipitation rates. (c) Movement of the position of the gravel front as a consequence of change in sea level. (d) Movement of the shoreline as a consequence of change in sea level.

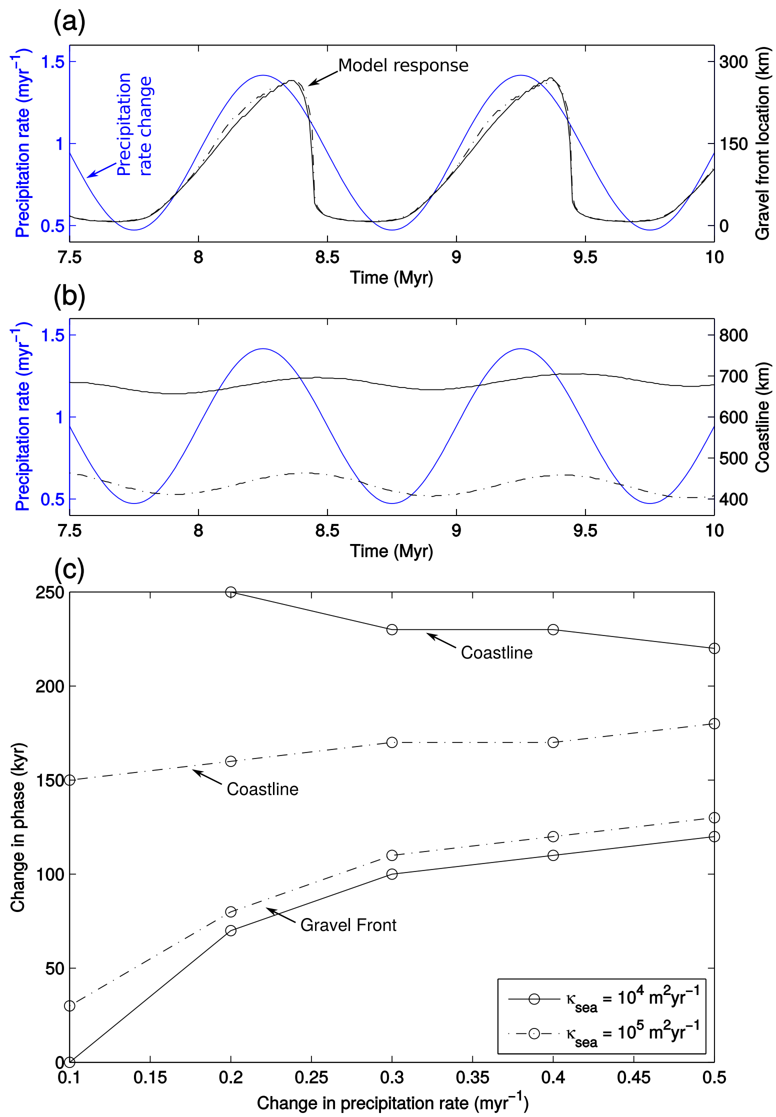

Figure 7: Response of the sediment transport model where $\kappa_{sea} = 10^4\,\mathrm{m}^2\mathrm{yr}^{-1}$ (dashed black lines) and $\kappa_{sea} = 10^5\,\mathrm{m}^2\mathrm{yr}^{-1}$ (solid black lines) to increasing magnitude of change in precipitation rates (blue lines). (a) Movement of the position of the gravel front as a consequence of a $\pm 50\,\%$ change in precipitation rates. (b) Movement of the shoreline as a consequence of a $\pm 50\,\%$ change in precipitation rates. (c) Delay in the peak response (i.e. timing of maximum regression) of the gravel front position and shoreline with respect to the peak in precipitation rates is plotted against the magnitude, relative to the mean, of change in precipitation rates. The gravel front is always upsystem of the shoreline. The shoreline for a 0.1 (10 %) change in precipitation rates with $\kappa_{sea} = 10^4\,\mathrm{m}^2\mathrm{yr}^{-1}$ is omitted as there was no periodicity in predicted shoreline trajectory.

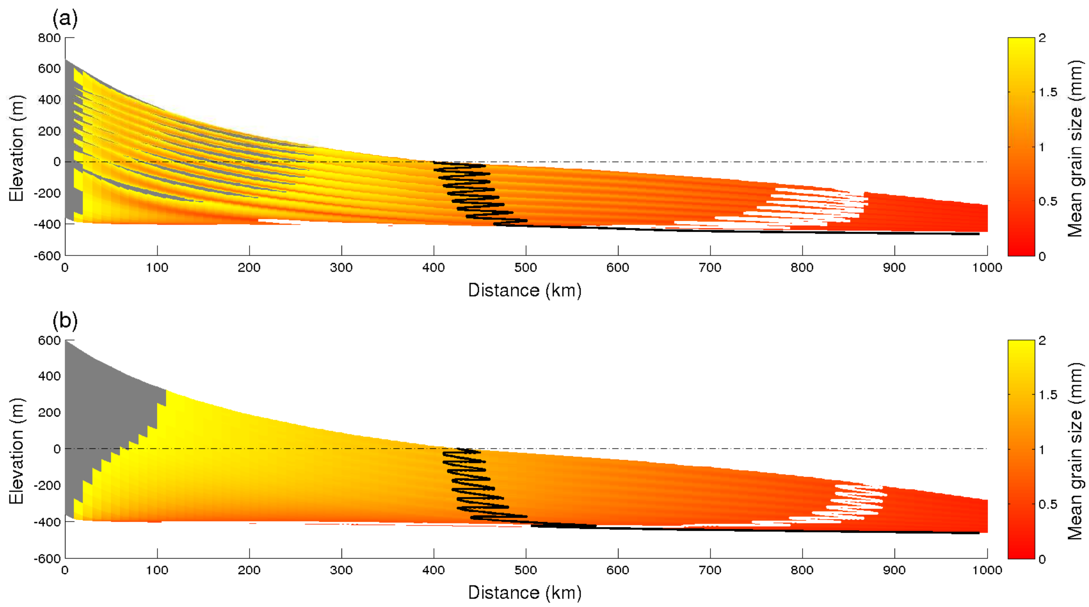

Figure 8: Model stratigraphic sections for oscillating precipitation rates and oscillating sea level. κ_{decay} (Equation 3) is held constant at $5 \times 10^4\,\mathrm{m}^{-1}$. (a) Grain size deposited for a model case where $\kappa_{sea} = 10^5\,\mathrm{m}^2\mathrm{yr}^{-1}$ and there is a $\pm 50\,\%$ change in precipitation rate about a mean of $1\,\mathrm{m\,yr}^{-1}$ with a period of 1 Myr. Regions of gravel grains are blocked out in gray. The mean grain size of grains finer than 2 mm in diameter is plotted, with the grain size of 0.5 mm displayed as a white contour that approximates the sand front. The shoreline position through time is marked as a solid black line, and the dashed black line marks sea level. (b) As part a, but where precipitation rates are held constant and sea level oscillates periodically by $\pm 10\,\mathrm{m}$.

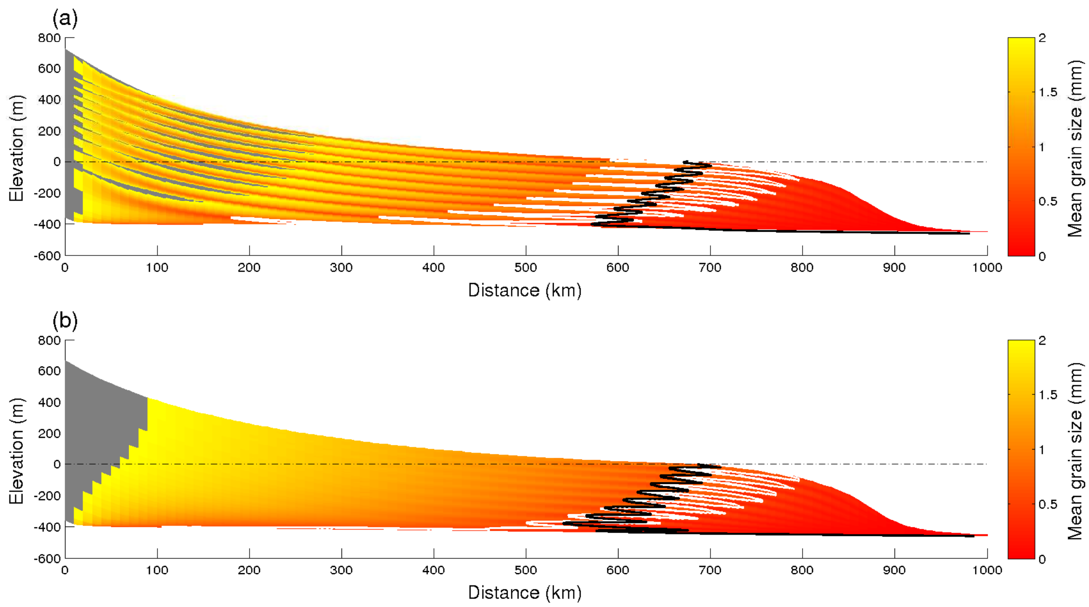

Figure 9: Model stratigraphic sections for oscillating precipitation rates and oscillating sea level. κ_{decay} (Equation 3) is held constant at $5 \times 10^4\,\mathrm{m}^{-1}$. (a) Grain size deposited for a model case where $\kappa_{sea} = 10^4\,\mathrm{m}^2\mathrm{yr}^{-1}$ and there is a $\pm 50\,\%$ change in precipitation rate about a mean of $1\,\mathrm{m\,yr}^{-1}$ with a period of 1 Myr. Regions of gravel grains are blocked out in gray. The mean grain size of grains finer than 2 mm in diameter is plotted, with the grain size of 0.5 mm displayed as a white contour that approximates the sand front. The shoreline position through time is marked as a solid black, and the dashed black line marks sea level. (b) As part a, but where precipitation rates are held constant and sea level oscillated periodically ± 10 m.

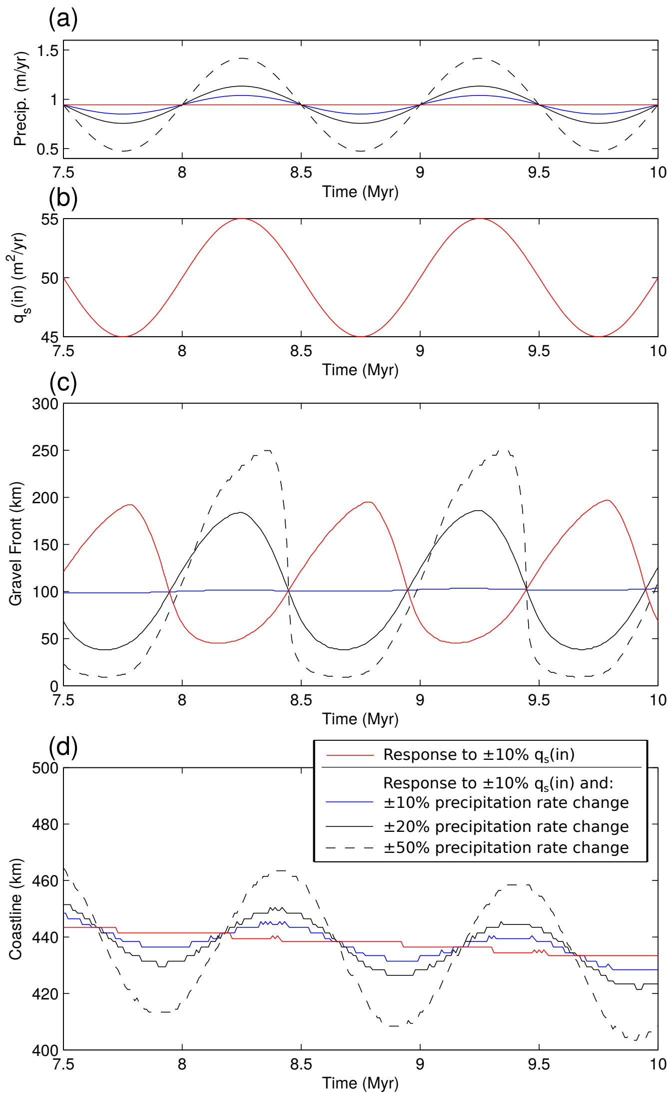

Figure 10: Response of the sediment transport model to change in input sediment flux, $q_s(in)$, and change in precipitation rates, α. (a) Modelled periodic oscillations in precipitation rate in parts c and d. (b) Modelled periodic oscillations in input sediment flux in parts c and d. (c) Movement of the position of the gravel front due to periodic oscillations in input sediment flux only (red line) and combinations of change in input sediment flux and precipitation (blue and black lines). (d) Movement of the shoreline due to periodic oscillations in input sediment flux only (red line) and combinations of periodic oscillations in input sediment flux and precipitation rate (blue and black lines).

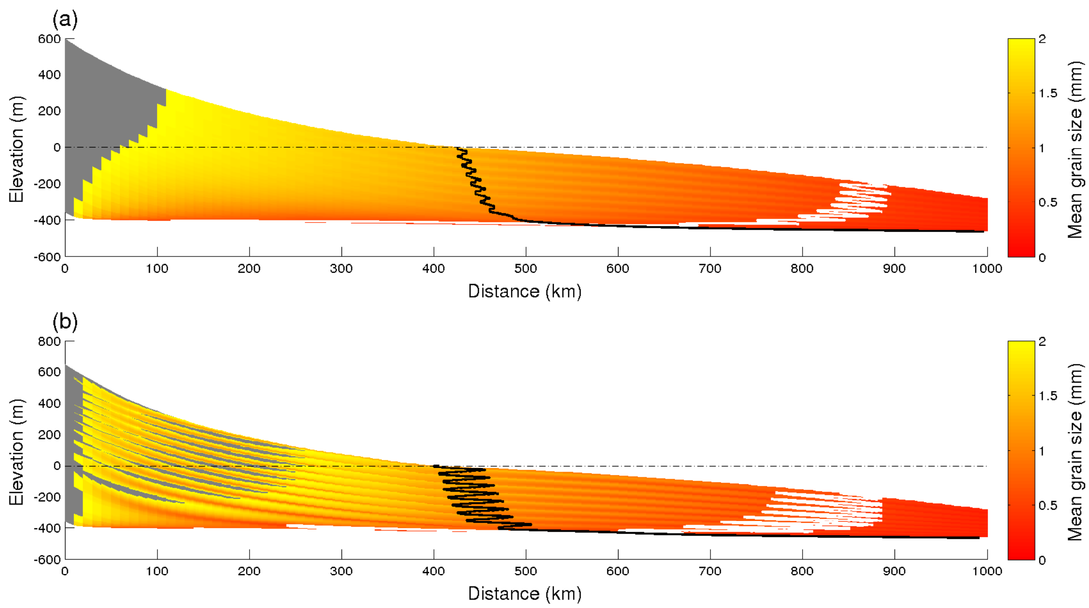

Figure 11: Model stratigraphic sections for oscillating precipitation rate combined with oscillating input sediment flux. κ_{decay} (Equation 3) is held constant at $5 \times 10^4\,\mathrm{m}^{-1}$. (a) Grain size deposited for a model case where $\kappa_{sea} = 10^5\,\mathrm{m}^2\mathrm{yr}^{-1}$ and there is a $\pm 10\,\%$ change in precipitation rates about a mean of $1\,\mathrm{m\,yr}^{-1}$ with a period of 1 Myr coupled with a $\pm 10\,\%$ change in input sediment flux around a mean of $50\,\mathrm{m}^2\mathrm{yr}^{-1}$. Regions of gravel grains are blocked out in gray. The mean grain size of grains finer than 2 mm in diameter is plotted, with the grain size of 0.5 mm displayed as a white contour that approximates the sand front. The shoreline position through time is marked as a solid black line, and the dashed black line marks sea level. (b) As part a, but for a $\pm 50\,\%$ oscillations in precipitation rates about a mean of $1\,\mathrm{m\,yr}^{-1}$ with a period of 1Myr, coupled with a $\pm 10\,\%$ oscillation in input sediment flux around a mean of $50\,\mathrm{m}^2\mathrm{yr}^{-1}$.

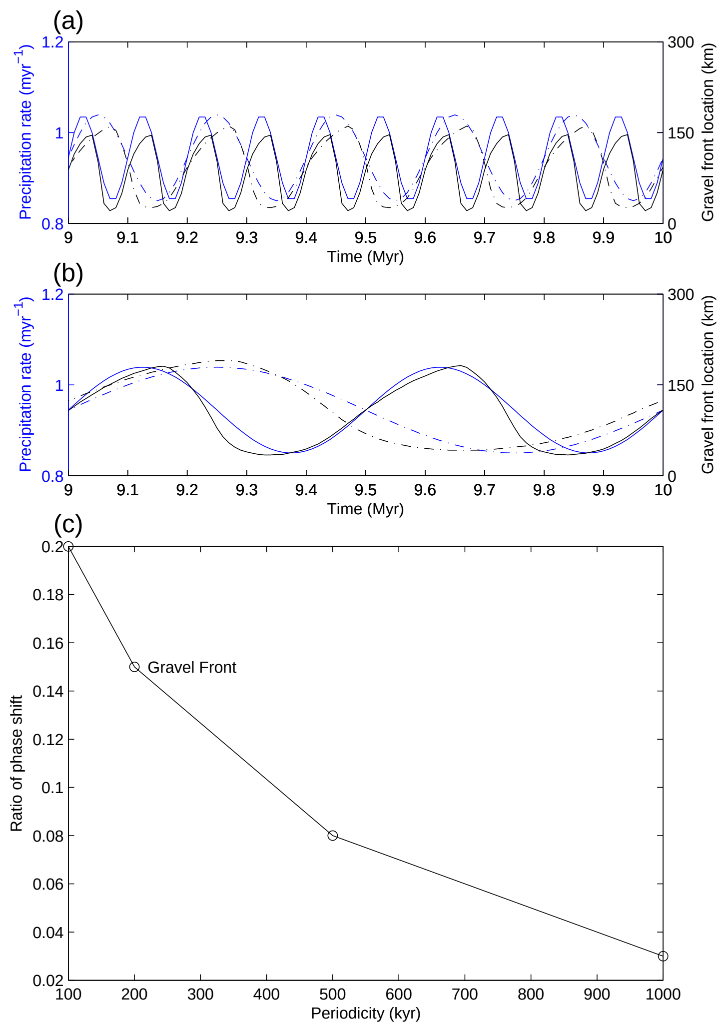

Figure 12: Response of the sediment transport model where $\kappa_{sea} = 10^5\,\mathrm{m^2yr^{-1}}$ to different frequencies of oscillations in precipitation rate (100, 200, 500 and 1000 kyr). (a) Precipitation rates (blue lines) and gravel front position (black lines) for 100 and 200 kyr oscillations (solid and dashed lines, respectively). (b) Precipitation rates (blue lines) and gravel front position (black lines) for 500 and 1000 kyr oscillations (solid and dashed lines, respectively). (c) Phase shift in response of the position of the gravel front relative to the period of precipitation rate change plotted against the frequency of precipitation-rate oscillations.

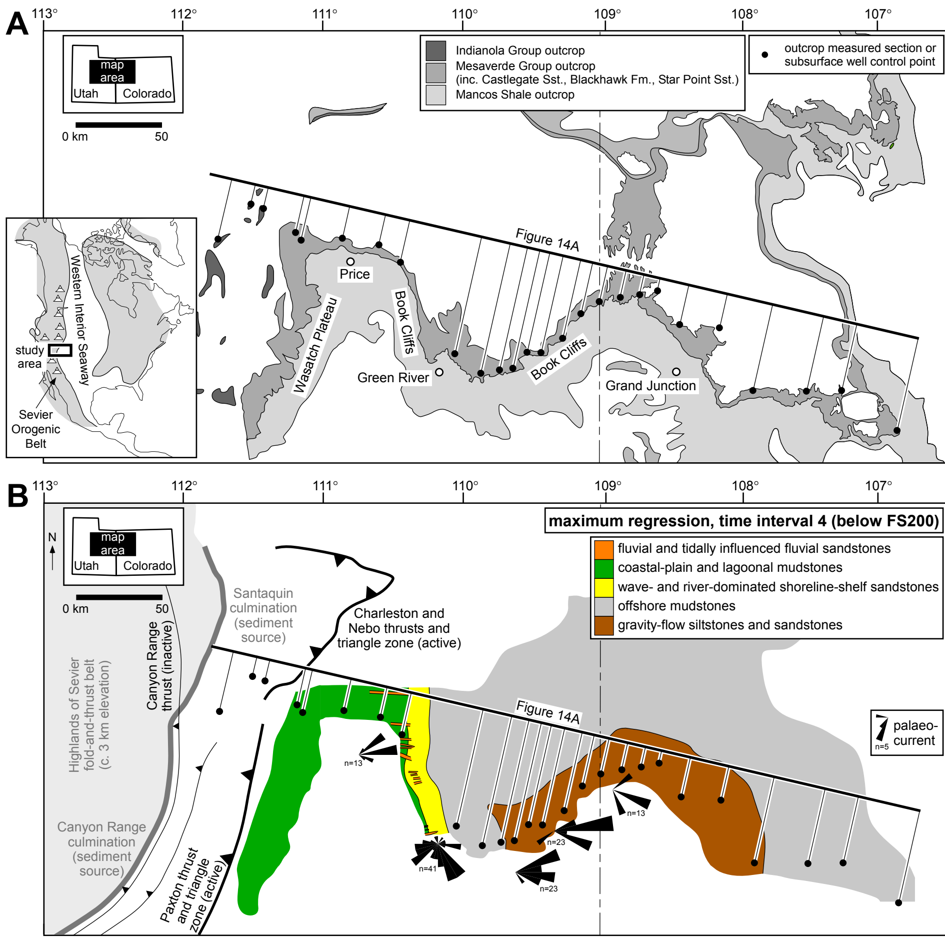

Figure 13: Maps showing (a) the extent and distribution of the outcrop belt that contains the Star Point – Blackhawk – Castlegate sediment-routing system deposits, and (b) facies-belt extent at maximum regression within time interval 4, between major flooding surfaces FS200 and FS100 (Figure 14), and the positions of tectonic features that influenced geomorphology, drainage, and sediment supply from the Sevier Orogen are shown (after Johnson, 2003; Horton et al., 2004; DeCelles and Coogan, 2006; Hampson et al., 2014). The inset map in part a shows the location of the study area on the western margin of the late Cretaceous Western Interior Seaway (after Kauffman and Caldwell, 1993).

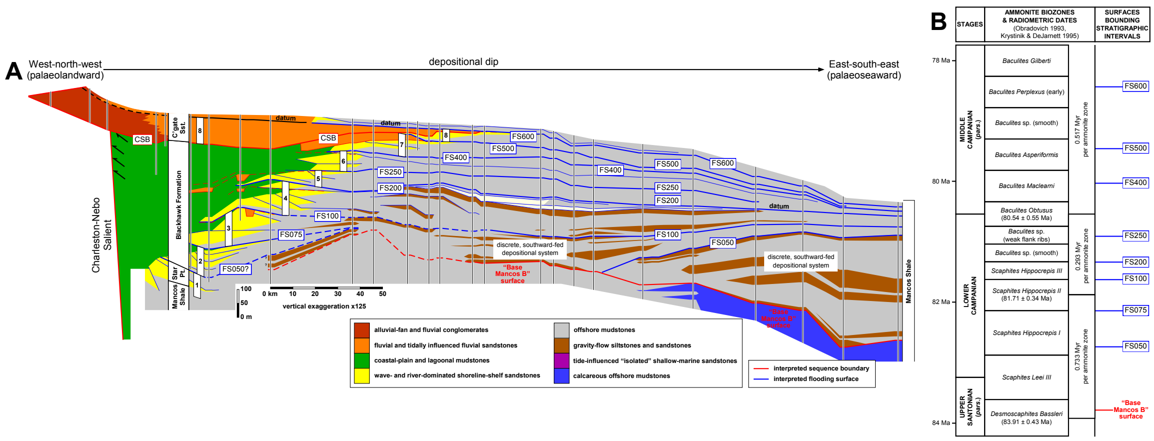

Figure 14: (a) Correlation panel illustrating stratigraphic architecture through the Book Cliffs outcrops and adjacent areas (after Horton et al., 2004; Hampson, 2010; Hampson et al., 2014 and references therein). Interpreted major flooding surfaces and erosional unconformities (sequence boundaries) are labelled. Deposits corresponding to time intervals 1-8 are indicated. Up-system correlation of the lower part of the Castlegate Sandstone (time interval 8) is after Robinson and Slingerland (1998a) and McLaurin and Steel (2000). A variety of stratigraphic surfaces are used as datum surfaces for different parts of the panel, and each surface is assigned the depositional dip of an eastward-dipping coastal plain or shelf profile where used as a datum. The panel is located in Figure 13. (b) Ammonite biostratigraphy, radiometric dates (Obradovich, 1993), and estimated ammonite biozone durations (Krystinik and DeJarnett, 1995) for the studied strata, showing the interpreted ages of major flooding.

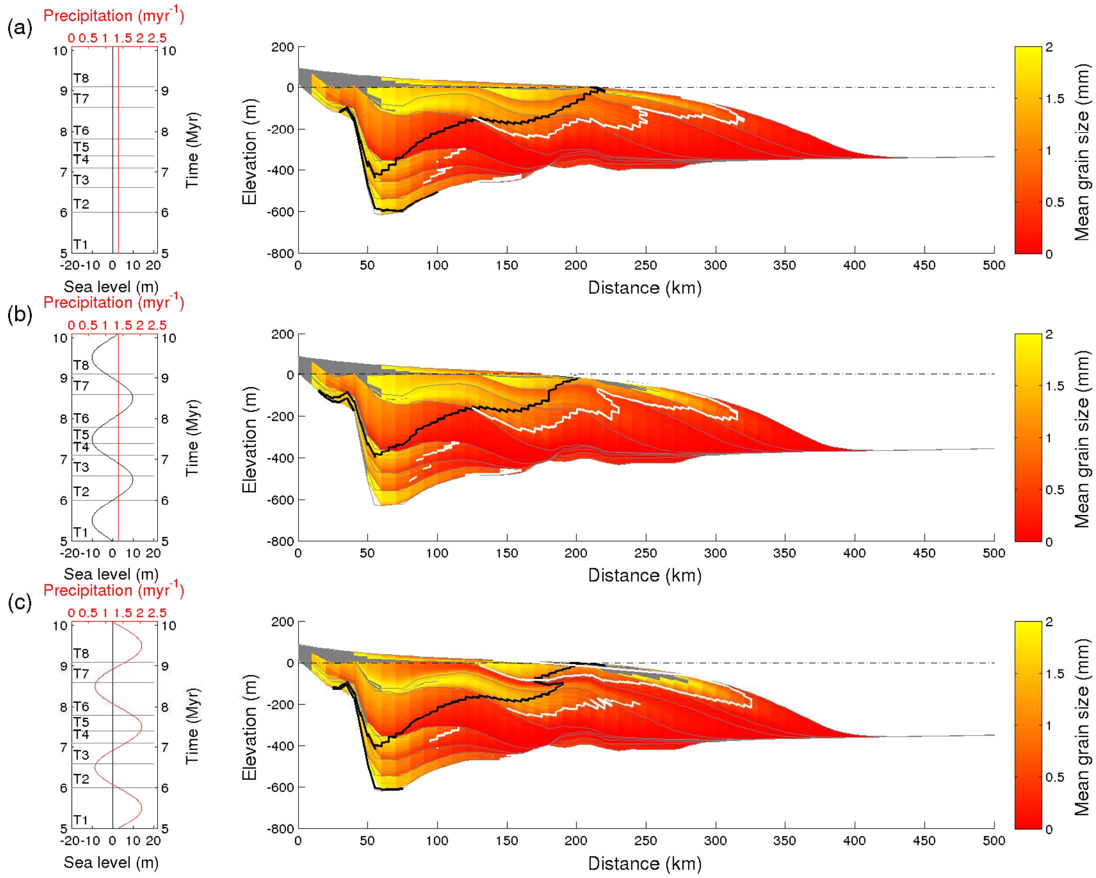

Figure 15: Synthetic strata for three models of the stratigraphic architecture in the Star Point – Blackhawk – lower Castlegate wedge, based on the Book Cliffs outcrops. (a) Predicted stratigraphic architecture assuming no change in sea level or precipitation rate ($1.4\,\mathrm{m\,yr^{-1}}$) throughout the model duration. (b) Predicted stratigraphic architecture assuming a 2 Myr periodic change in relative sea-level of amplitude $\pm 10\,\mathrm{m}$. (c) Predicted stratigraphic architecture assuming a 2 Myr periodic change in precipitation rates of amplitude $\pm 50\,\%$. Regions of gravel grains are blocked out in gray. The mean grain size of grains finer than 2 mm in diameter is plotted, with the grain size of 0.5 mm displayed as a white contour that approximates the sand front. The shoreline position through time is marked as a solid black line, and the dashed black line marks sea level.

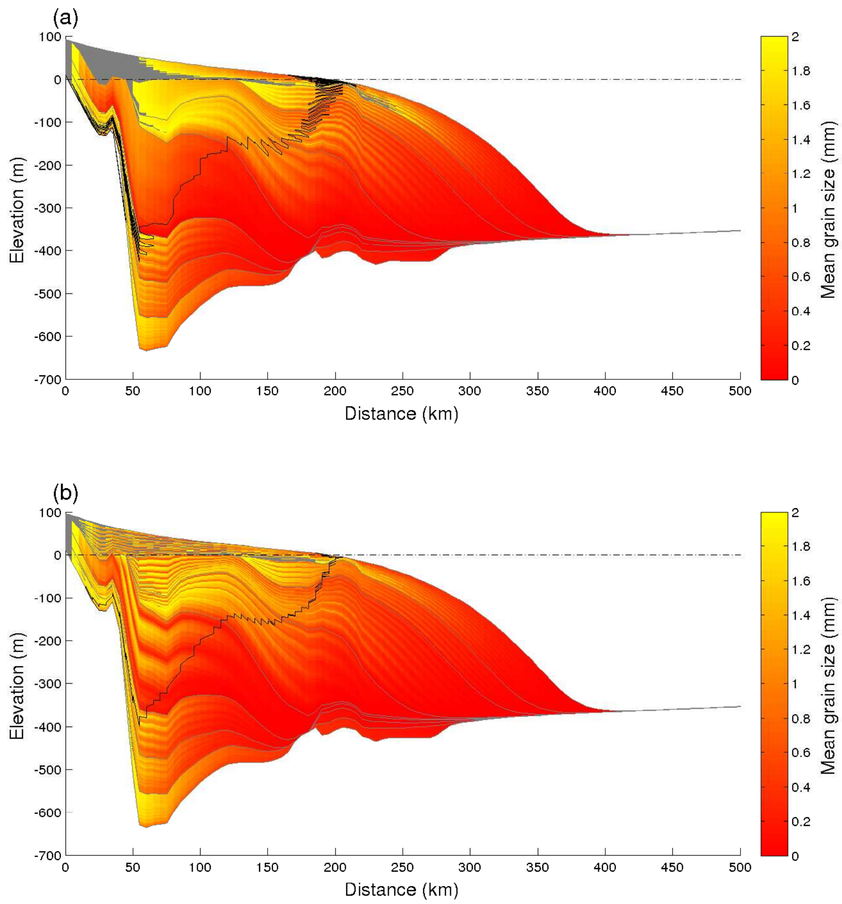

Figure 16: Synthetic strata for two models of the stratigraphic architecture in the Star Point – Blackhawk – lower Castlegate wedge, based on the Book Cliffs outcrops. (a) Predicted stratigraphic architecture assuming a 100 kyr periodic oscillation in relative sea-level of amplitude ±10 m. (b) Predicted stratigraphic architecture assuming a 100 kyr periodic oscillation in precipitation rate of amplitude ±50 %. Regions of gravel grains are blocked out in gray. The mean grain size of grains finer than 2 mm in diameter is plotted. The shoreline position through time is marked as a solid black line, and the dashed black line marks sea level.

Table 1: List of model parameters

Parameter	Description	Value
κ	Linear hill slope diffusion coefficient	1 m^2yr^{-1}
c	Fluvial transport coefficient	10^{-1}
n	Transport exponent	1
κ_{sea}	Subaqueous diffusion coefficient	10^4 to 10^5 $m2yr^{-1}$
κ_{decay}	Subaqueousl diffusion decay coefficient	$5x10^3$ to $5x10^5$ m^{-1}

Table 2: Gravel front and shoreline trajectory analysis

Figure	κ_{sea} (m^2yr^{-1})	κ_{decay} (m^{-1})	Forcing	Gravel front trajectory	Shoreline trajectory
3a	10^5	$5x10^4$	Steady sea level, precipitation rate and input sediment flux	Steady progradation at ~4 $kmMyr^{-1}$	Steady retrogradation at ~4 $kmMyr^{-1}$
3b	10^4	$5x10^4$	Steady sea level, precipitation rate and input sediment flux	Steady progradation at ~4 $kmMyr^{-1}$	Steady progradation at ~12 $kmMyr^{-1}$
5a	$5x10^4$	$5x10^3$	Steady sea level, precipitation rate and input sediment flux	Steady progradation at ~8 $kmMyr^{-1}$	Steady progradation at ~13 $kmMyr^{-1}$
5b	$5x10^4$	$5x10^5$	Steady sea level, precipitation rate and input sediment flux	Steady progradation at ~4 $kmMyr^{-1}$	Steady progradation at ~14 $kmMyr^{-1}$
8a	10^5	$5x10^4$	Oscillating precipitation rate (±50%), steady sea level and input sediment flux	Cycles of progradation and retrogradation over a distance of ~270 km	Cycles of progradation and retrogradation over 50 km. Long term retrogradation of order 5 $kmMyr^{-1}$.
9a	10^4	$5x10^4$	Oscillating precipitation rate (±50%), steady sea level and input sediment flux	Cycles of progradation and retrogradation over a distance of ~270 km	Cycles of progradation and retrogradation over 20 km. Long term retrogradation of order 10 $kmMyr^{-1}$.
8b	10^5	$5x10^4$	Oscillating sea level (±10 m), steady precipitation rate and input sediment flux	Steady progradation	Cycles of progradation and retrogradation over 40 km. Long term retrogradation of order 5 $kmMyr^{-1}$.
9b	10^4	$5x10^4$	Oscillating sea level (±10 m), steady precipitation rate and input sediment flux	Steady progradation	Cycles of progradation and retrogradation over 50 km. Long term retrogradation of order 10 $kmMyr^{-1}$.
11a	10^5	$5x10^4$	Oscillating precipitation rate (±10%), and input sediment flux (±10 %), steady sea level	Steady progradation	Cycles of progradation and retrogradation over 20 km. Long term retrogradation of order 5 $kmMyr^{-1}$.
11b	10^5	$5x10^4$	Oscillating precipitation Rate (±50%), and input sediment flux (±10 %), steady sea level	Cycles of progradation and retrogradation over a distance of ~270 km	Cycles of progradation and retrogradation over 50 km. Long term retrogradation of order 5 $kmMyr^{-1}$.

Table 3: Model input conditions for application to the Star Point – Blackhawk – lower Castlegate – Manacos sediment routing system

Time Period	T0	T1	T2	T3	T4	T5	T6	T7	T8
Duration (Myr)	5	1	0.6	0.5	0.3	0.4	0.8	0.5	1
Input Sediment Flux (m^2yr^{-1})	7	7	14.1	23.2	119.7	47	32.7	19.1	19
Gravel Fraction (%)	0.7	0.7	0.8	0.5	0.1	0.3	0.5	0	18.8
Sand Fraction (%)	41.4	41.4	37.6	37.2	20.4	15.4	20.7	22.3	40.1
Fines Fraction (%)	57.8	57.8	61.6	62.4	79.5	84.3	78.9	77.7	41.1
Distance (km)	Subsidence rate (mmyr-1)								
0	0.15	0	0	0	0	0	0	0	0
9000	0.15	0	0	0	0	0	0	0	0.05
28000	0.15	0	0	0	0	0	0	0	0.13
35000	0.15	0	0	0	0	0	0	0	0.1
57000	0.15	0.1	0.12	0.16	0.23	0.15	0.19	0	0.1
61000	0.15	0.1	0.12	0.16	0.23	0.15	0.19	0	0.09
74000	0.15	0.1	0.12	0.16	0.23	0.15	0.19	0	0.08
84000	0.15	0.1	0.12	0.16	0.23	0.15	0.14	0	0.07
106000	0.15	0.1	0.08	0.16	0.23	0.15	0.09	0	0.06
120000	0.15	0.1	0.07	0.16	0.23	0.15	0.08	0	0.05
163000	0.15	0.09	0.02	0.1	0.23	0.13	0.08	0.12	0.04
180000	0.15	0.07	0	0.06	0.17	0.13	0.08	0.12	0.03
191000	0.15	0.11	0.07	0.08	0.1	0.1	0.08	0.06	0.03
198000	0.15	0.11	0.07	0.08	0.1	0.1	0.08	0.06	0.02
204000	0.15	0.11	0.07	0.08	0.1	0.1	0.08	0.06	0.01
212000	0.1	0.11	0.07	0.08	0.1	0.1	0.08	0.06	0.01
222000	0.1	0.11	0.07	0.08	0.1	0.1	0.08	0.06	0.03
230000	0.1	0.12	0.07	0.08	0.1	0.1	0.08	0.06	0.03
239000	0.1	0.11	0.07	0.08	0.1	0.1	0.08	0.06	0.03
250000	0.1	0.11	0.07	0.08	0.1	0.1	0.08	0.06	0.03
260000	0.1	0.11	0.07	0.08	0.1	0.1	0.08	0.06	0.03
270000	0.1	0.11	0.07	0.08	0.1	0.1	0.08	0.06	0.03
287000	0.1	0.08	0.07	0.08	0.1	0.1	0.08	0.06	0.03
310000	0.1	0.07	0.07	0.08	0.1	0.1	0.08	0.06	0.03
338000	0.1	0.06	0.07	0.08	0.1	0.1	0.08	0.06	0.03
368000	0.1	0.04	0.07	0.08	0.1	0.1	0.08	0.06	0.03
388000	0.1	0.04	0.07	0.08	0.1	0.1	0.08	0.06	0.03
425000	0.1	0.04	0.07	0.08	0.1	0.1	0.08	0.06	0.03